SYNTHESIS, STRUCTURAL AND MAGNETIC PROPERTIES OF $CoSn_xFe_{2-x}O_4$ and $M_{0.5}Ni_{0.5}Fe_2O_4$ (M=Mg, Ca, Sr, Ba) NANOFERRITES

by

Nokwanda Precious Ngema

BSc, BSc(Hons) (Univerity of Limpopo-Medunsa)

Submitted in fulfilment of the academic requirements for the degree of Master of Science in the School of Chemistry and Physics, University of KwaZulu-Natal, Durban, South Africa.

April 2017

Abstract

The study of the magnetic and structural properties of $CoSn_xFe_{2-x}O_4$ ($0 \leqslant x \leqslant 1$) and $M_{0.5}Ni_{0.5}Fe_2O_4$ (M= Mg, Ca, Sr, Ba) synthesized by the glycol-thermal route has been carried out. The structural properties were investigated using Fourier transform infrared (FTIR) and X-ray diffraction (XRD) measurements. XRD and FTIR data confirmed the formation of a single phase cubic spinel structure in the samples synthesized. The Scherrer formula helped in determining the crystallite sizes of the oxides found in the ranges between 10 nm and 23 nm. The lattice parameters of the $CoSn_xFe_{2-x}O_4$ ($0 \leqslant x \leqslant 0.5$) were observed to be increasing with an increase in x. The lattice parameters in the $M_{0.5}Ni_{0.5}Fe_2O_4$ (M= Mg, Ca, Sr, Ba) samples were increasing with the ionic radii of the cations. The value of particle size estimated from high resolution transmission electron microscopy (HRTEM) was found to be similar to that from XRD patterns for a sample. High resolution electron microscopy (HRSEM) micrographs of $x = 0.5$ and $x = 0.1$ indicated a uniform distribution of particles with different sizes. The small particles indicated by SEM images compared well with nanoscale crystallites size estimated from XRD data. The magnetic measurements were performed using Mössbauer spectroscopy at room temperature for all the samples. The Mössbauer spectra recorded have been found to be indicative of ordered magnetic spin phase for the $M_{0.5}Ni_{0.5}Fe_2O_4$ nanoferrites. The hyperfine field showed a decrease in the Sn-doped samples as x was increasing. The fitting of the sextets and a doublet in the ferrites was an indicator of the ferrites being in ferromagnetic and paramagnetic state. Magnetization measurements were obtained using the Vibrating sample magnetometer (VSM). The coercive field, saturation magnetization and remanent magnetization were obtained at room temperature. Some properties such as lattice parameters, XRD densities, unit cell volume and coercive fields of the $CoSn_xFe_{2-x}O_4$ ferrites showed a subsequent increase as x increased. A good correlation between the coercive field and particle size for the $CoSn_xFe_{2-x}O_4$ samples was determined. The magnetization properties of the $M_{0.5}Ni_{0.5}Fe_2O_4$ (M= Mg, Ca, Sr, Ba) appeared to decrease as the ionic radii of the metal ions were increasing. The substitution of Ba however showed an increase due to the site occupancy of the doped metal ions at different lattice sites. Nanocrys-

talline $Co_{0.5}Ni_{0.5}Fe_2O_4$ ferrite was also studied. The samples were annealed from 300 °C to 900 °C. The broadening of the XRD peaks at lower temperatures account for the nanosized nature of the samples. The temperature dependence of the magnetic properties such as coercive field, saturation magnetization, remanent magnetization and squareness of the hysteresis loops were investigated. The sample transformed from single-domain to multi-domain configuration at particle size of about 31 nm. The sample annealed at 700 °C exhibits a maximum coercivity, at 300 K.

PREFACE

The experimental work described in this dissertation was carried out in the Condensed Matter Physics Lab, School of Chemistry and Physics, Westville Campus, University of KwaZulu-Natal, Durban under the supervision of Dr. T. Moyo and Dr. J. Z. Msomi. The content of this work have not been submitted in any form to another university or institution. Credit has been given where use of the work of others is made.

DECLARATION 1 - PLAGIARISM

I, Nokwanda Precious Ngema declare that

1. The research reported in this dissertation, except where otherwise indicated, is my original research.

2. This dissertation has not been submitted for any degree or examination at any university.

3. This dissertation does not contain other person's data, pictures, graphs or other information, unless specifically acknowledged as being sourced from other persons.

4. This dissertation does not contain other persons writings, unless specifically acknowledged as being sourced from other researchers. When other written sources have been quoted, then:

5. Their words have been re-written but general information attributed to them has been referenced.

6. Where their exact words have been used, their writing has been placed in italics and inside quotation, and referenced.

7. This dissertation does not contain text, graphics or tables copied and pasted from internet, unless specifically acknowledged, and the source being detailed in the dissertation and in the reference sections.

Signed: ..... Date: April 2017

Name: Nokwanda Precious Ngema

DECLARATION 2 - PUBLICATIONS

1. The effect of Temperature on the structure and Magnetic properties of $Co_{0.5}Ni_{0.5}Fe_2O_4$ spinel nanoferrite, Hafiz M.I. Abdallah, Thomas Moyo, **Nokwanda Ngema**, Journal of Magnetism and Magnetic Materials 394 (2015) 223-228.

2. Synthesis and magnetic properties of Sn-doped $CoFe_2O_4$ nanoferrites, **N.P Ngema**, J.Z. Msomi, T. Moyo, A. Strydom, D. Britz, Journal of superconductivity and Novel Magnetism, (2016) doi:10.1007/s10948-016-3786-6

Signed: ..... Date: April 2017

Name: Nokwanda Precious Ngema

Dedication

To my mother, MaSimelane Magutshwa. I thank God to have given me a strong mother who encourages me to be better no matter what. Your unconditional love and prayers kept me going and I will be forever grateful for that. To dad, Ngema Dlokovu thank you for all the support. My brother Qiniso, if you had not sacrificed anything for me I would not be here. Thank you a lot. To my sisters Zakithi and Nomalungelo, your presence in my life made things easier for me, I love you and thank you a lot for standing in the gap when I was not there. Olwethu and Zenokuhle, this one is for you my girls. You are my greatest gifts. I hope you will grow and be proud of me. God bless all of you for your contributions in my life.

Contents

Abstract iii

Preface iv

Declaration v

Publication vi

Dedication vii

Table of contents vii

Acknowledgments x

List of Figures xiii

List of Tables xiv

1 Introduction **1**

1.1 Ferrites 1

1.1.1 Spinel structure of ferrites 2

1.1.2 Synthesis of ferrites 3

1.2 Applications of ferrites 4

1.3 Motivation for the current work 4

1.4 Dissertation outline 5

2 Magnetism and magnetic order in solids **7**

2.1 Origin of magnetism 7

2.2 Classification of magnetic materials 9

2.2.1 Diamagnetism 9

2.2.2 Paramagnetism 10

2.2.3 Ferromagnetism 13

2.2.4 Antiferromagnetism 16

2.2.5 Ferrimagnetism 17

3 Mössbauer spectroscopy 19

3.1 Introduction 19

3.1.1 Principles of the Mössbauer effect 19

3.2 Hyperfine interactions 23

3.2.1 Isomer shift 23

3.2.2 Quadrupole splitting 24

3.2.3 Magnetic hyperfine interaction 25

4 Experimental techniques 26

4.1 Introduction 26

4.1.1 Glycol-thermal 26

4.1.2 X-ray diffraction 29

4.1.3 FTIR 31

4.1.4 HRTEM 33

4.1.5 Magnetization measurements 34

5 Structural and magnetic properties of $CoSn_xFe_{2-x}O_4$ nanoferrite 36

5.1 Introduction 36

5.2 Experimental details 37

5.3 Results and discussion 38

5.3.1 XRD results 38

5.3.2 Morphology study 40

5.3.3 FTIR results 41

5.3.4 Mössbauer measurements 42

5.3.5 Magnetization measurements 45

5.4 Conclusion 50

6 Synthesis structural and magnetic properties of $M_{0.5}Ni_{0.5}Fe_2O_4$ nanoferrites 51

6.1 Introduction 51

6.2 Results and discussion 52

6.2.1 XRD results 52
6.2.2 FTIR 55
6.2.3 Magnetization 56
6.2.4 Mössbauer Spectroscopy results 56
6.3 Conclusion 60

7 General conclusions **62**

Bibliography **64**

Acknowledgments

I would like to thank the following people for their contributions and sacrifices to make this work a success:

Dr. T. Moyo for the invaluable supervision and the support throughout the period of this work.

Dr. J. Z. Msomi for the support, encouragement and patience throughout the period of this work.

My fellow research colleagues (Dr. Nadir Osman, Itegbeyogene Ezekiel and Sanele Dlamini) for the support and all their contributions to my work.

I am grateful to Sasol Pty Ltd for providing me with the student grant.

The magnetic measurements undertaken were made possible by equipment grant to the Condensed Matter Physics Lab at Westville Campus, UKZN by the National Research Foundation (NRF) of South Africa and the University of KwaZulu-Natal.

List of Figures

1.1.1 Spinel unit cell crystal structure [11]. 3

2.2.1 Magnetization dependence on magnetic field and susceptibility dependence on temperature of a diamagnetic material [39]. 10
2.2.2 Atomic dipoles for a paramagnetic material. 11
2.2.3 Magnetization dependence on magnetic field and susceptibility dependence on temperature of a paramagnetic material [39]. 13
2.2.4 Magnetic moments of a ferromagnetic material [43]. 13
2.2.5 Graphical presentation of equation (2.2.20) and (2.2.21) [45]. 15
2.2.6 Magnetic moments of a ferrimagnetic material [43]. 17

3.1.1 Mössbauer spectroscopy used for measurements. 20
3.1.2 Schematic demonstration of ^{57}Co nuclear decay [47]. 20
3.1.3 Recoilless emission or absorption of a gamma ray [49]. 21
3.1.4 Graphical representation of resonant absorption and recoilless emission [50]. 22
3.2.1 Isomer shifts, electrical quadrupole splitting and magnetic hyperfine splitting on nuclear energy levels [50]. 24

4.1.1 The PARR 4843 stirred pressure reactor. 27
4.1.2 Synthesis schedule for the PARR 4843 stirred pressure reactor. 28
4.1.3 Rigaku Miniflex 600 XRD diffractometer using Cu-K_α radiation (λ = 1.5818 Å). 30
4.1.4 XRD PANalytical Emperian diffractometer using Co-K_α radiation (λ = 1.7903 Å). 30

4.1.5 Schematic diagram of the optical layout of a Michelson interferometer [57]. 32
4.1.6 PerkinElmer Spectrum 100 FT-IR spectrometer. 32
4.1.7 HRTEM taken at the Electron Microscopy unit at UKZN-Westville campus. 33
4.1.8 LakeShore Cryotronics 735 Vibrating Sample Magnetometer. 35

5.3.1 X-rays patterns for the $CoSn_xFe_{2-x}O_4$ ferrites obtained by Cu-K_α radiation source for $x = 0$ and by Co-K_α for $0.1 \leq x \leq 1.0$. 39
5.3.2 HRTEM images of $x = 0.5$ and $x = 0.1$. 40
5.3.3 HRSEM micrographs of $x = 0.5$ and $x = 0.1$. 41
5.3.4 FTIR spectrum of $CoSn_{0.5}Fe_{1.5}O_4$. 41
5.3.5 Mössbauer spectra for $CoSn_xFe_{2-x}O_4$ samples measured at room temperature. 43
5.3.6 Hyperfine fields at different sites for $CoSn_xFe_{2-x}O_4$ plotted as a function of particle size. 43
5.3.7 Hyperfine fields at different sites for $MnFe_2O_4$ plotted as a function of particle size [72]. 44
5.3.8 Hysteresis loops of $CoSn_xFe_{2-x}O_4$ measured at room temperature. . . 46
5.3.9 Magnetization as a function of magnetic field recorded from 4-250 K for x=0.5. 47
5.3.10 Zero field cooling magnetization curves. 48
5.3.11 Correlation between coercive fields at 300 K with crytallite sizes for $x = 0$, 0.1, 0.5. 49

6.2.1 XRD patterns of $M_{0.5}Ni_{0.5}Fe_2O_4$ (M= Mg, Ca, Sr and Ba). 53
6.2.2 Correlation between particle size and pressure for $M_{0.5}Ni_{0.5}Fe_2O_4$ where (M = Mg, Ca, Sr and Ba). 54
6.2.3 FTIR spectra for $M_{0.5}Ni_{0.5}Fe_2O_4$ (M= Mg, Ca, Sr and Ba). 55
6.2.4 Hysteresis loops for $M_{0.5}Ni_{0.5}Fe_2O_4$ (M= Mg, Ca, Sr and Ba). 57
6.2.5 The variation of coercive field with particle size for $M_{0.5}Ni_{0.5}Fe_2O_4$ (M = Mg, Ca, Sr and Ba). 58

6.2.6 Mossbauer spectra for $M_{0.5}Ni_{0.5}Fe_2O_4$ nanoferrites. 59

List of Tables

5.3.1 The lattice parameters (a), crystallite sizes (D), X-ray densities (ρ) and unit cell volume (V) of the ferrites. 40

5.3.2 Isomer shifts (δ), quadrupole splitting (ε), hyperfine fields (H), line widths (Γ) and Fe fraction (f) for $CoSn_xFe_{2-x}O_4$ (x = 0, 0.1, and 0.5). 45

5.3.3 Coercive field H_C, magnetization M_s and residual magnetization M_R measured at 300 K. 46

6.2.1 The lattice parameters (a), crystallite sizes (D), X-ray densities (ρ) of the $M_{0.5}Ni_{0.5}Fe_2O_4$ (M= Mg, Ca, Sr and Ba) ferrites. 54

6.2.2 Coercive field H_C, magnetization M_s and residual magnetization M_R measured at 300 K. 58

6.2.3 Isomer shifts (δ), quadrupole splitting (ε), hyperfine fields (H), line widths (Γ) and Fe fraction (f) for $CoSn_xFe_{2-x}O_4$ (x = 0, 0.1, and 0.5). 60

Chapter 1

Introduction

1.1 Ferrites

The name ferrite originated from the Latin word ferrum meaning iron. Ferrites are defined as a group of oxides with the chemical formula $M\mathrm{Fe_2O_4}$ where M is a divalent metal ion such Zn^{2+}, Cd^{2+}, Mg^{2+}, Ni^{2+}, Fe^{2+}, Cu^{2+} or a combination of these ions in the case of mixed ferrites. Ferrites may also possess the combined properties of magnetic materials and insulators. The ferrites can be divided into different groups namely spinel, garnet, ortho ferrites and hexaferrites [1]. The crystal structure is that of a mineral spinel $\mathrm{MgAl_2O_4}$ which was first determined by Bragg and Nishikawa in 1915 where Mg ions are replaced by the divalent M ions and Al by Fe [2, 3]. The structure consists of a closed lattice of oxygen ions forming tetrahedral (A) and octahedral (B) sites [4]. The chemical formula can also be written in the form $\mathrm{AB_2O_4}$ where A and B are metal cations on the tetrahedral and octahedral sites. The properties of ferrites are dependent on several factors such as type and distribution of metal cations at the interstitial sites, crystallite size and synthesis technique [5]. Amongst the properties in the magnetized state, the spin moments may or may not be aligned in the same direction [6]. The magnetic properties of ferrites are due to the interactions in the tetrahedral (A) and octahedral (B) sites. In this chapter some details of the crystal structure, synthesis and applications of ferrites are discussed. A brief motivation for the present study is also presented.

1.1.1 Spinel structure of ferrites

Figure 1.1.1 shows the crystal structure where Fe ions can be located at tetrahedral (A) and octahedral (B) sites surrounded by the oxygen ions. The oxygen ions are packed close together in a face-centered cubic arrangement resulting in smaller spaces between them. In the unit cell of oxygen ions, 32 are octahedral and 64 are tetrahedral of which 16 and 8, respectively are occupied by metal ions [4]. Depending on the arrangement of the ions and cation distribution in the interstitial sites, the structure may be referred to as normal, inverse and in some cases mixed spinel. In a normal spinel, the divalent ions occupy the tetrahedral sites and trivalent ions occupy the octahedral site. Some examples of the normal spinel are $ZnFe_2O_4$ and $CdFe_2O_4$. The intermediate structures between normal and inverse spinel structures can be characterized by a degree of inversion, λ. In such cases the distribution of cations amongst the tetrahedral and octahedral sites is expressed by $(M_{1-2\lambda})[M_{2(1-\lambda)}]$ with the normal brackets representing the A site and square brackets the B site, respectively. The value of λ is temperature dependent in the range from 0 to 0.5 with $\lambda = 0$ for a normal spinel and $\lambda = 0.5$ for an inverse spinel [7]. The examples of inverse spinel ferrites are $NiFe_2O_4$ and $CuFe_2O_4$ [8]. In the nickel ferrite, the spinel structure is in its ideal state with all Ni^{2+} ions in the B-sites and Fe^{3+} ions being distributed between A and B sites [9]. Mixed ferrites can be produced where M in the structure is a combination of two or more divalent ions. Some common examples of the mixed ferrites are Mg-Zn, Ni-Zn and Co-Ni ferrites. Some interesting features of the spinel ferrites includes their strong dependence of properties on the state of chemical order and on the cation distribution. The magnetic order of the ferromagnetic spinels is known to be due to the super-exchange interaction mechanism that occurs between the metal ions in the tetrahedral A sites and octahedral in the B site. The difference of the magnetic moments of the ions in the B site and those in the A site give rise to the magnetization [10].

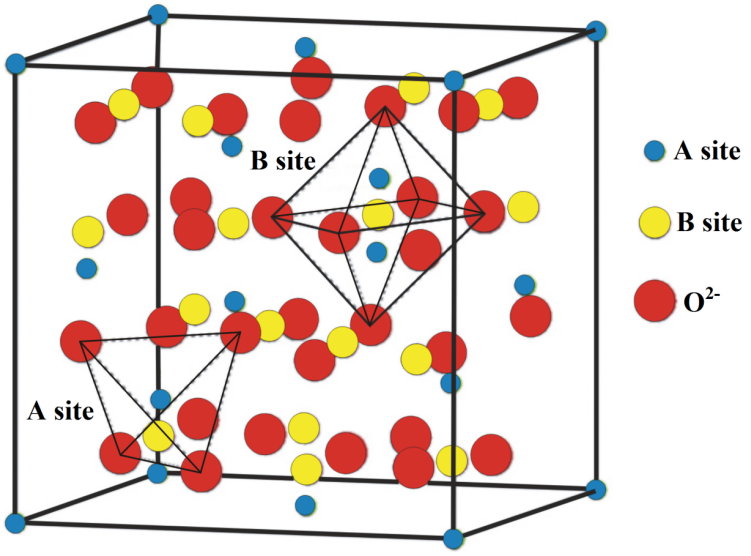

Figure 1.1.1: Spinel unit cell crystal structure [11].

1.1.2 Synthesis of ferrites

In order to obtain the desired results and properties, selecting an appropriate synthesis method is critical. Researchers use several synthesis methods such as conventional ceramic method, sol-gel method, co-precipitation, combustion and high energy ball milling to study the properties of nanomaterials. The conventional ceramic method has the disadvantage of prolonged annealing time at high temperature which causes some loss of the sample due to evaporation and can unbalance the stoichiometric composition. The mechanical milling may introduce impurities and as a result the final properties may be inconsistent and not re-producible. The ceramic method tend to produce ferrites with low surface area which limits their applications [12]. Wet chemical methods are usually the preferred method in the production of nanomaterials as they provide better control of the morphology and particle size with minor impurities [13]. Wet chemical methods include hydrothermal [14], glycol-thermal [15], co-precipitation [16], sol-gel [17] and combustion [18]. In these methods, metal chlorides or nitrates are used as starting materials which are mixed by continuously stirring in deionized water. A base such as ammonium hydroxide (NH_4OH) is added

to the mixture to form a precipitate. The precipitate is then dispersed in deionised water or ethylene glycol and heated to allow the reaction to take place. After heating the mixture is filtered and dried. The ferrites produced by wet chemical methods are expected to have minimal impurities. That is why the preferred method used for this study is the glycol thermal method.

1.2 Applications of ferrites

Ferrites exhibit a wide range of electromagnetic properties that are useful for for a variety of technological applications. Since these materials can be prepared as room temperature insulating ferromagnets by varying the divalent and trivalent ions into the spinel lattice, they play a significant role in various technological devices [19, 20]. Based on the magnetic properties, ferrites are used in permanent magnets and memory storage devices. Spinel ferrites have interesting electrical properties that are suited for high frequency applications with potential applications in new areas such as medicine, electronics and electrical engineering [21]. Nickel ferrite ($NiFe_2O_4$) is a soft ferrite used in microwave devices, catalysis, photomagnetic materials, gas sensors and site specific drug delivery and the cobalt ferrite ($CoFe_2O_4$) is a hard ferrite which has attracted a lot of attention for its applications in biomedicine, catalysis, microwave absorbers, magnetic inks and high-density magnetic memories [22, 23, 24, 25, 26].

1.3 Motivation for the current work

Magnetic properties of ferrites are influenced by their cation distribution amongst the interstitial sites. Synthesis method, composition, sintering time and sintering temperature influence the cation distribution and hence the magnetic properties. Ionic sizes and cation valency also play a role in cation distribution [9]. $NiFe_2O_4$ possesses an inverse spinel structure and is a well-known magnetic material which has been studied due to a combination of different properties such as excellent corrosion resististance, chemical and mechanical stability, high Curie temperature,

low coercivity, high electrical resistivity and high saturation magnetization [27, 28, 29]. The most significant difference with $CoFe_2O_4$ is the high coercivity associated with high anisotropy of Co ions. Several researchers have studied properties of $NiFe_2O_4$ and $CoFe_2O_4$ in their pure forms after syntheses by different methods. Many attempts have been made to study the changes in the properties with cation substitution in both $NiFe_2O_4$ and $CoFe_2O_4$.

Ugendar *et al.* [30] have reported on the synthesis, magnetic and electrical properties of a series of bulk $CoFe_{2-x}$ Sn_xO_4 with (x = 0.025, 0.05, 0.075) prepared by solid state reaction at 1200 °C in order to study the effects of doping by non-magnetic Sn^{4+} ions. In this study we will investigate on the properties nanosized $CoFe_{2-x}$ Sn_xO_4 with (x = 0, 0.1, 0.5) prepared by low temperature synthesis.

Replacing nickel by divalent metal ions such as Zn^{2+}, Mg^{2+}, Cd^{2+} and Ca^{2+} significantly affects the properties and have been widely reported [26, 31]. There seems to be not much emphasis on the systematic studies of substitutions by alkaline earth metals in ferrites. Naidu and Madhuri [32] have studied the structural and magnetic properties of $Ni_xMg_{1-x}Fe_2O_4$ prepared by double sintering using microwaves and Vigneswari and Raji [33] studied $Ni_{0.5}Ca_{0.5}Fe_2O_4$ produced by co-precipitation method. In this study we also intend to investigate the effects of composition and change in magnetic properties of $NiFe_2O_4$ substituted with Mg, Ca, Sr and Ba which are alkaline earth metals and are in Group 2 in the periodic table. We are also particularly interested in how the synthesis pressure in the pressure reactor affects the particle sizes and how these affect the properties. All the samples prepared for this study were synthesized by glycol-thermal method from pure metal chlorides at 200 °C.

1.4 Dissertation outline

This dissertation is arranged in the following order: chapter 1 includes some basic introduction to ferrites and motivation for the dissertation. A discussion on the fundamentals of magnetics order in solids is given in chapter 2. The experimental techniques used for the synthesis, structural and magnetic characterization of the

samples are presented in chapter 3 and 4. Chapters 5 and 6 are devoted to the experimental results for all the samples synthesized and the final conclusions of the work are given in chapter 7.

Chapter 2

Magnetism and magnetic order in solids

This chapter will give some background information on magnetism and its origin and also give a brief discussion on the different types of magnetic order in solids. This will help in understanding better and analysing the magnetic properties in chapter 4 and 5.

2.1 Origin of magnetism

The origin of magnetism lies in the orbital and spin motions of electrons and how the electrons interact with one another. Magnetic properties of the spinel ferrite are mainly due to the interaction of species on tetrahedral A sites and Octahedral B sites controlled by substitution of trivalent or tetravalent ion in the host spinel lattice [6]. The interaction between magnetic moments via intermediary oxygen ions is referred to as superexchange interaction and results in anti-parallel arrangement with net non-zero magnetization [34]. This type of order is called ferrimagnetism. The magnetic behaviour of materials can be classified into the following five major orders: Diamagnetism, paramagnetism, ferromagnetism, ferrimagnetism and anti-ferromagnetism. There are two types of motion of electrons in atoms, one is the motion of the electrons in an orbit around the nucleus, similar to the motion of the planets in our solar system around the sun, and the other is the spin of the electrons

around its axis, analogous to the rotation of the Earth about its own axis [26]. The circular motion of electrons around the nucleus and their intrinsic spin results in the existence of magnetic moments. The moments can be permanent or induced under the effect of a magnetic field. The current I is constituted by the moving electron is associated with a magnetic moment defined as

$$\vec{\mu} = IA \tag{2.1.1}$$

where A is the area of the closed loop with a magnitude of πr^2. For the electron moving with an angular speed ω then

$$I = -ef = \frac{e\omega}{2\pi} \tag{2.1.2}$$

where f is knows as the frequency of rotation. The magnetic moment can then be defined as

$$\mu = -\frac{e}{2m_e} l \tag{2.1.3}$$

where l is the orbital angular momentum of the electron. From quantum mechanics the z-component of the angular momenta of $(\vec{l})$ leads to

$$\mu_{l_Z} = -\left(\frac{e\hbar}{2m_e}\right) m_l = -\mu_B m_l \tag{2.1.4}$$

where $\hbar$ is called the reduced Planck constant (h) defined as $\hbar = h/2\pi$, the magnetic quantum number $m_l = 0, \pm 1, \pm 2, \pm 3, ...)$ and μ_B is smallest non-zero fundamental value of μ with the value of 9.247×10^{-24} J/T defined as

$$\mu_\beta = \left(\frac{e\hbar}{2m_e}\right) \tag{2.1.5}$$

known as the Bohr magneton. The magnetic moment due to the intrinsic spin for an electron is given by

$$\mu_s = -\frac{e}{2m_e} gs \tag{2.1.6}$$

with g being the Landé g factor having an experimental value of 2.002322 for pure electron spin and s being the intrinsic spin of the angular momentum. According to

Russel Saunders coupling, the orbital momenta of the electrons in an atom couple is given by

$$L = \sum_{i=1}^{n} l_i \tag{2.1.7}$$

and similarly the resultant spin angular moment S is

$$S = \sum_{i=1}^{n} s_i. \tag{2.1.8}$$

The total angular moment J is taken as a result of coupling of L and S through spin-orbit interaction. From Hund's Rule the magnitude of the magnetic moment of an atom is given as

$$\mu_j = \mu_B g \sqrt{J(J+1)} \tag{2.1.9}$$

with g factor for a free atom is defined as

$$g = 1 + \frac{J(J+1) + S(S+1) - L(L+1)}{2J(J+1)}. \tag{2.1.10}$$

2.2 Classification of magnetic materials

Materials may be classified by their response to externally applied magnetic fields as diamagnetic, paramagnetic, or ferromagnetic. These magnetic responses differ greatly in strength, arrangement and orientation of the magnetic moments [35, 36]. This section will give a brief description on the classes of the magnetic materials.

2.2.1 Diamagnetism

Diamagnetism is an inherent result of the orbital motions of the electrons in the magnetic field. The motions are altered by the field to produce induced magnetic moments in the direction opposite to the applied field described by a negative susceptibility [37]. The diamagnetic contribution to the magnetism arises from all electrons. However, its contribution is usually very small [37]. This is usually suppressed by other magnetic affects in a sample. The susceptibity χ of the diamagnetic materials [38] may be defined as

$$\chi = -\mu_0 n \frac{e^2}{6m_e} \sum_i^Z < r_i^2 > \tag{2.2.1}$$

with Z being the atomic number, r_i the orbital radii of the electrons, μ_0 the magnetic permeability, m_e electron mass and n the number of atoms per unit volume. Diamagnetic materials may be used to align the magnetic field induced liquid crystals. Figure 2.2.1 illustrate the magnetization dependence on magnetic field and susceptibility dependence on temperature of a diamagnetic material. The figure shows the magnetic response of the diamagnetic material and also from the figure the magnetic susceptibility χ of a diamagnetic material is negative and constant as a function of temperature.

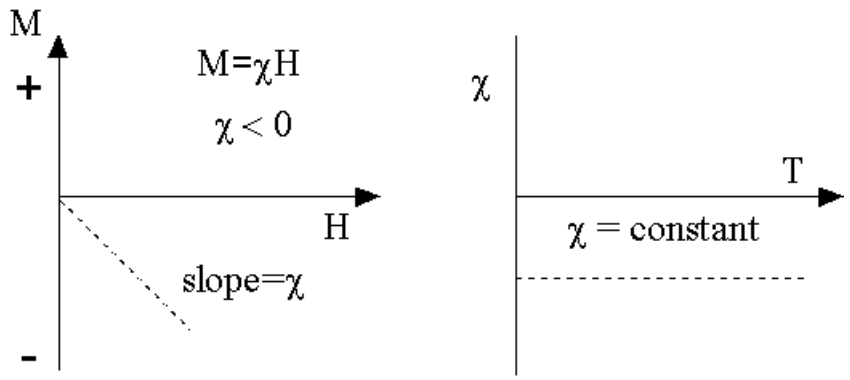

Figure 2.2.1: Magnetization dependence on magnetic field and susceptibility dependence on temperature of a diamagnetic material [39].

2.2.2 Paramagnetism

The term paramagnetism is used to describe the low and linear increase in flux density with an increase in the magnetic field [40]. Whe the electron spin ans orbital magnetic moments are not cancelled completely the paramagnetic materials possess a permanent dipole moment. The moments align by rotating towards the direction of the field in the presence of an applied field and are randomly oriented in the absence of the field. The net magnetization is acquired by the material [37], as illustrated in Figure 2.2.2.

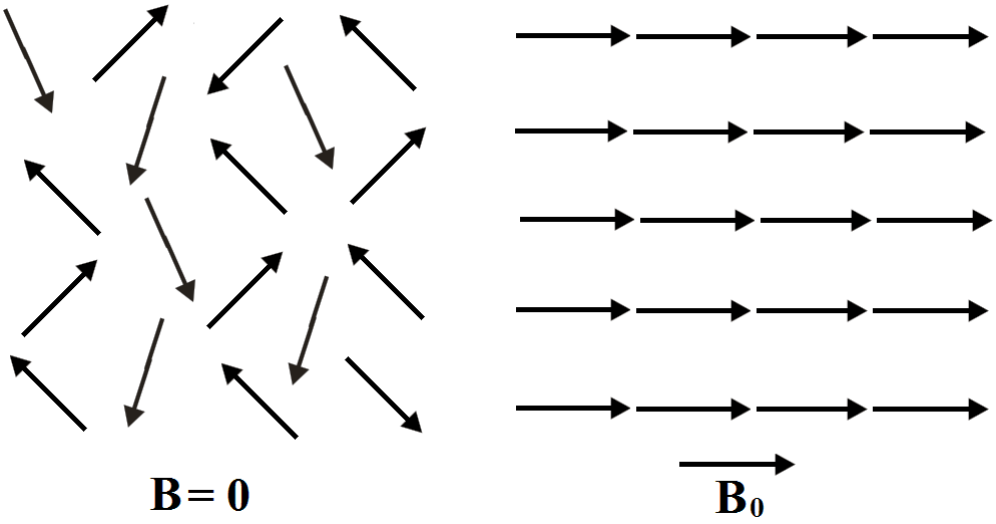

Figure 2.2.2: Atomic dipoles for a paramagnetic material.

In the case where there is no magnetic field, the paramagnetic material will not show any magnetization. Magnetic field and the temperature plays an important role in the paramagnetic materials in order to determine the magnetization of the material. The energy of a magnetic moment in an applied magnetic field B_0 is described by

$$E_{mJ} = -\vec{\mu}.\vec{B_0} = -g\mu_B m_J B_0 \tag{2.2.2}$$

where $\vec{\mu}_j$ is the magnetic moment and m_j is the quantum number part of the set $-J, J(J-1), (J-2), \cdots, (1-J), J$ and g is the Lande's g-factor given by

$$g = 1 + \frac{J(J+1) + S(S+1) - L(L+1)}{2J(J+1)}. \tag{2.2.3}$$

The average of the magnetic moment $< \mu_J >$ is then given by

$$< \mu_J >= \sum g m_J \mu_B P(E_{mJ}) \tag{2.2.4}$$

where $P(E_{mJ})$ is the probability of the occupation energy level (E_{mJ}) given in with reference to the Maxwell-Boltzmann distribution as

$$P(E_{mJ}) = \frac{e^{-E_{mJ}/k_B T}}{\sum m_J e^{-E_{mJ}/k_B T}} \tag{2.2.5}$$

where k_B is the Boltzmann constant.

The average magnetic moment is given as

$$< \mu_J >= g\mu_B JF(j,x) \tag{2.2.6}$$

where

$$x = \frac{g\mu_B JB_0}{k_B T}. \tag{2.2.7}$$

$F(J,x)$ is called the Brillouin function and is given as

$$F(J,x) = \frac{2J+1}{2J}\coth\left(\frac{(2J+1)x}{2J}\right) - \frac{1}{2J}\coth\left(\frac{x}{2J}\right) \tag{2.2.8}$$

which is the asymptotic to the Langevin function for every J and to $tanhx$ when $J = \frac{1}{2}$ and $g = 2$ [6, 41]. The Brillouin function varies from zero when applied field is zero to unity for infinite field. Thus the saturation magnetization for a paramagnetic solid is $M_{max} = Ng\mu_B J$ [41]. The magnetization for non-interacting moments per unit volume is then given by

$$M = \frac{ng^2\mu_B J(J+1)B_0}{3k_B T} \tag{2.2.9}$$

leading to the Curie law susceptibility expressed as

$$\chi = \frac{C}{T} \tag{2.2.10}$$

with C known as the Curie constant, expressed as

$$C = \frac{n\mu_0 g^2\mu_B^2 J(J+1)}{3k_B}. \tag{2.2.11}$$

When interactions between magnetic moments in a paramagnet are significant, the susceptibility is expressed by the modified Curie law known as the Curie-Weiss law

$$\chi = \frac{C}{T-\theta_P} \tag{2.2.12}$$

where θ_P is the paramagnetic Curie temperature.

The dependence of susceptibility on temperature is shown in Figure 2.2.3. The figure shows that the increase in temperature T causes a decrease in the susceptibility χ. The magnetic susceptibility χ of a paramagnetic material is positive.

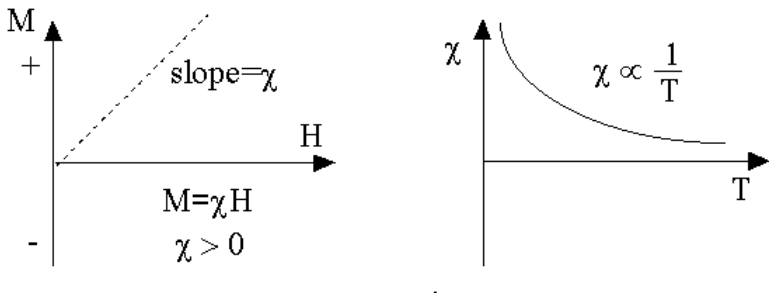

Figure 2.2.3: Magnetization dependence on magnetic field and susceptibility dependence on temperature of a paramagnetic material [39].

2.2.3 Ferromagnetism

Ferromagnetism is a type of magnetism whereby the material has a spontaneous magnetic moment even in zero magnetic field and is due to the electron spin with little or no contribution from orbital motion of the electrons [42]. Co-operative interaction of large numbers of atomic spins in domains is the result of the permanent magnetic moment in the ferromagnetic materials. The regions in which all the spins are aligned in the same direction, is shown in Figure 2.2.4.

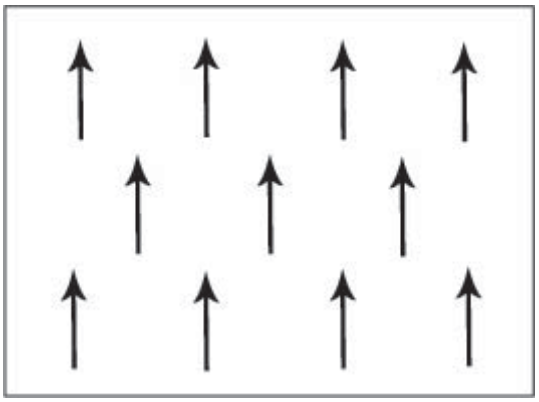

Figure 2.2.4: Magnetic moments of a ferromagnetic material [43].

Below the Curie temperature (T_C), the magnetic moments of the atoms are magnetically ordered. Above T_C the magnetic moments point in random directions and the material behaves like a paramagnet because the thermal energy is large enough to overcome the cooperative ordering of the magnetic moments. In this case, the

susceptibility obeys the Curie-Weiss law [44]. The variation of the magnetization with temperature is explained by the Weiss mean field theory. Weiss (1907) supposed that in addition to any externally applied field, there is an internal molecular field in a ferromagnet proportional to its magnetization

$$B_{int} = \lambda M_s \tag{2.2.13}$$

where λ is a molecule field coefficient. The assumption by Weiss was based on the knowledge that magnetic moments are ordered under the influence of an internal magnetic field B_{int}. The magnetic binding energy is the one responsible for the alignment of the moments at $T = 0$ K, while the thermal energy at T_C will be sufficient to kill the perfect magnetic order that is existing. For a magnetic moment

$$\mu_B B_{in} \sim k_B T_C. \tag{2.2.14}$$

For $T_c \sim 100$ K, B_{int} should be at least 100 T which is a much larger field that can be produced through the magnetic dipole interaction. In the case where there is an externally applied magnetic field, the effective magnetic field in the sample is given as

$$B_{eff} = B_0 + B_{int} = B_0 + \lambda M_s. \tag{2.2.15}$$

Similar to a paramagnet, the magnetization of a ferromagnet in an applied field can be given in terms of the Brillouin function where

$$M_s(B, T) = ng\mu_B JF(J, y). \tag{2.2.16}$$

The ratio of the Zeeman energy to thermal energy is now defined as

$$y = \frac{g\mu_B J(B_0 + \lambda M_s}{k_B T)} \tag{2.2.17}$$

The magnetization will stay finite even for $B_0 = 0$. At $B_0 = 0$ and $T > 0$ the spontaneous magnetization can be given as

$$M_s(0, T) = M_s(0, 0)F(J, y) \tag{2.2.18}$$

where $M_s(0,0)$ is the saturation magnetization and y is given by

$$y = \frac{g\mu_B J M_s(0,T)}{k_B T}. \tag{2.2.19}$$

The spontaneous magnetization from equation 2.2.18 can be described in terms of the reduced magnetizations

$$\frac{M_s(0,T)}{M_s(0,0)} = F(J,y) \tag{2.2.20}$$

and

$$\frac{M_s(0,T)}{M_s(0,0)} = \left(\frac{k_B T}{ng^2\mu_B^2\lambda J^2}\right)y. \tag{2.2.21}$$

The variation of the reduced magnetization as a function of y is shown in Figure 2.2.5. The curve C1 represents equation (2.2.21) varies proportionally with temperature. The point of intersection between C1 and $F(J,y)$ represents the ferromagnetic state. The Weiss theory predicts the collapse magnetization at T_C but the theory does not account for the origin of the internal field and the reduction in magnetization with increasing temperature for $T << T_C$.

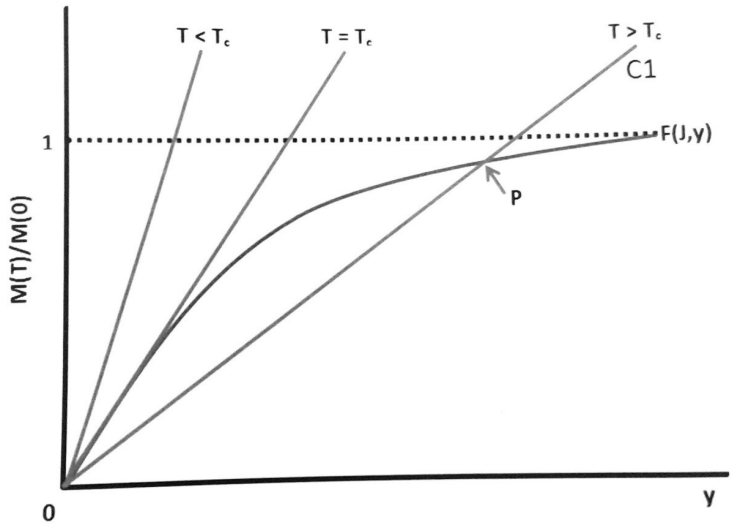

Figure 2.2.5: Graphical presentation of equation (2.2.20) and (2.2.21) [45].

2.2.4 Antiferromagnetism

In an antiferromagnet material, the magnetic moments line up so that the adjacent moments are aligned in opposite direction [44]. The moments result zero net magnetization [42]. Above the Néel temperature, the material becomes paramagnetic exhibiting Curie-Weiss behaviour. The antiferromagnet structure is made up of two atomic sublattices A and B with saturation magnetization M_A and M_B in opposite directions. At absolute zero temperature ($T = 0$ K), each sublattice has maximum saturation magnetization that decreases as the temperature increases similar to a ferromagnet. The internal magnetic field at each sublattice is given by

$$B_{in}^{A} = \lambda_{AA} M_A + \lambda_{AB} M_B \tag{2.2.22}$$

$$B_{in}^{B} = \lambda_{BB} M_B + \lambda_{BA} M_A. \tag{2.2.23}$$

The molecular field coefficients λ_{AB} and λ_{BA} correspond with the first nearest neighbors. The second nearest neighbor have these molecular field coefficients λ_{AA} and λ_{BB} respectively. With the application of the mean-field theory, the magnetization at each sublattice M_A and M_B can be determined in terms of the Brillouin function $F(J, x)$ so that.

$$M_i = \frac{n}{2} g \mu_B J F(J, x) \tag{2.2.24}$$

where i is the identity of the sublattice A or B and $x_i = \frac{g u_B J}{k_B T}(B_0 + B_{in}^{i})$. In the case where the is no applied field ($T \leqslant T_N$), the net magnetization is

$$\vec{M} = \vec{M_A} + \vec{M_B} = 0 \tag{2.2.25}$$

when $T > T - N$, the magnetization $\vec{M}$ depends on the applied field B_0 with an effective field B_{eff}^{i} and is expressed as

$$B_{eff}^{A} = B_0 + B_{in}^{A} = B_0 + \lambda_{AA} M_A + \lambda_A B M_B \tag{2.2.26}$$

and

$$B_{eff}^{B} = B_0 + B_{in}^{B} = B_0 + \lambda_{BB} M_B + \lambda_B A M_A \tag{2.2.27}$$

The susceptibility of an antiferromagnet at $T > T_N$ obeys the Curie-Wiess law

$$\chi = \frac{C}{T - \theta_P} \tag{2.2.28}$$

with θ_P mathematically defined as

$$\theta_P = \frac{C'(\lambda_{AA} + \lambda_{BB})}{2\mu_0}. \tag{2.2.29}$$

In an antiferromagnet $\theta_P < 0$. The susceptibility at $T < T_N$ magnetization depends whether the applied field is perpendicular or parallel to the orientation of the spins.

2.2.5 Ferrimagnetism

Ferrimagnetic materials possess a permanent magnetic moment in the absence of an external field and a large permanent magnetization due to an incomplete cancellation of the magnetic dipole moments [46]. This is similar to the antiferromagnetic alignment of the magnetic moments. However the adjacent moments of the ferrimagnets are usually of different magnitude, such that the larger of the two moments tends to align with the applied magnetic field while the smaller moment aligns opposite to the field [37]. Figure 2.2.6 shows the representation of the magnetic structure in a ferrimagnetic material.

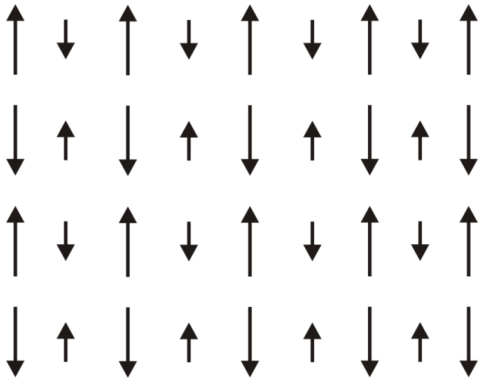

Figure 2.2.6: Magnetic moments of a ferrimagnetic material [43].

The net saturation magnetization can be modelled by the equation

$$M = M_A - (1 - \lambda)M_B \tag{2.2.30}$$

where $M_A \neq M_B$. The ferrimagnetism can occur when $\lambda \neq 0$, $\frac{1}{2}$ or 1. The net magnetization will always be non-zero except in cases where the magnetization of the two sublattices cancel out at $T_{comp} < T_C$, where T_{comp} is called the compensation temperature. Above T_C, the magnetization at each sublattice is given by

$$M_A = \left(\frac{C_A}{T}\right)(\lambda_{AA}M_A + \lambda_{AB}M_B + B_0) \tag{2.2.31}$$

and

$$M_B = \left(\frac{C_B}{T}\right)(\lambda_{AB}M_A + \lambda_{BB}M_B + B_0) \tag{2.2.32}$$

where λ_{AA}, λ_{AB} and λ_{BB} are the Weiss coefficients representing the inter- or intra-sublattice reactions.

Chapter 3

Mössbauer spectroscopy

3.1 Introduction

Mössbauer spectroscopy is a technique used to provide information in many areas of science such as Physics, Chemistry, Biology and Metallurgy. It can give very precise information about the chemical, structural, magnetic and time-dependent properties of a material. It is based on the 1958 discovery by Rudolf Mössbauer that it is possible for a nucleus of Ir^{191} to decay without recoil from its first excited state to its ground state by γ-ray emission [6]. This is now referred to as the Mössbauer effect. Mössbauer discovered that the resonant absorption increases with decreasing in temperature. The Fe^{57} isotope with an in incomplete filled $3d$ shell is usually used to study the magnetic materials by the Mössbauer effect. This means all the materials containing Fe can therefore be studied by Mössbauer spectroscopy. Figure 3.1.1 shows the instrument used for the current study.

3.1.1 Principles of the Mössbauer effect

Mössbauer effect is due to the nuclear resonant emission or absorption of gamma rays [6, 42]. It relies mostly on the Fe^{57} isotope after Co^{57} decays by electron capture. The ^{57}Co decays to the excited state $I_{ex} = 5/2$ of ^{57}Fe by nucleus electron capture (EC). This state in not stable because the ^{57}Fe nuclei can subsequently decay directly to the I_g (ground state of ^{57}Fe) with probability 9% or to the excited state $I_{ex} =$

3/2 with a probability of 91% and therefore the state is considered to be unstable [47]. The decay process is illustrated in Figure 3.1.2.

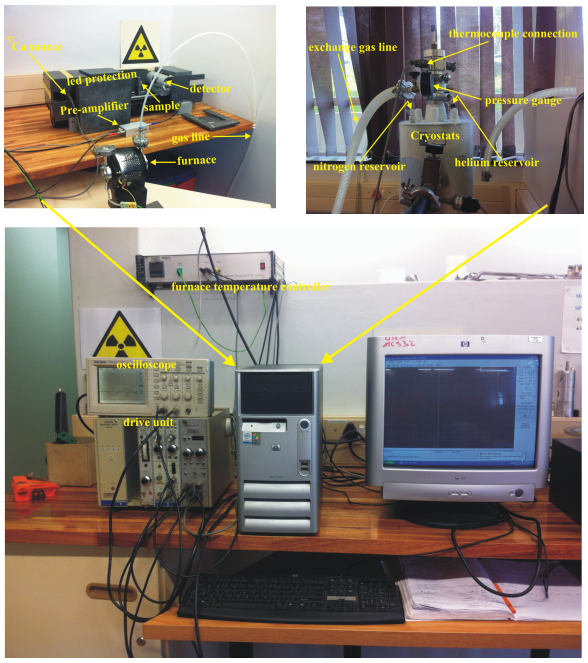

Figure 3.1.1: Mössbauer spectroscopy used for measurements.

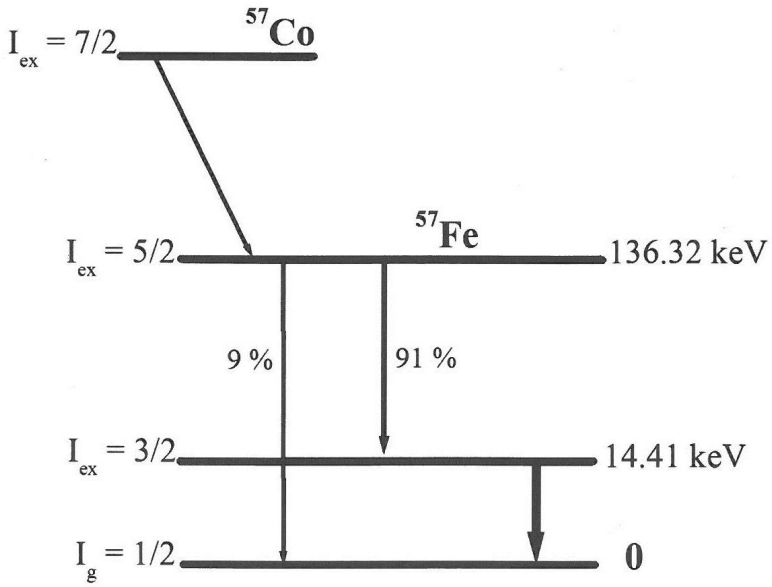

Figure 3.1.2: Schematic demonstration of ^{57}Co nuclear decay [47].

The decay from $I_{ex} = 3/2$ to $I_{ex} = 1/2$ produce γ-rays with energies of 14.41 keV

which are associated with ^{57}Fe Mössbuer spectroscopy. When a free nucleus at rest in an excited state with an energy E above the ground state emits a photon of energy $E_\gamma = pc$ it will receive a recoil momentum $-p$ and the nuclei recoil due to conservation of momentum with recoil energy E_R is then given by

$$E_R = \frac{{E_\gamma}^2}{2Mc^2} \tag{3.1.1}$$

where M is the mass of the nucleus and c is the speed of light. The recoil of free nuclei in the emission and absorption of a gamma ray is shown in Figure 3.1.3. However, when the nuclei are embedded in a completely rigid lattice, the recoil momentum in the case of emitting or absorbing a γ-ray is taken up by the solid as a whole. In this case the recoil energy is reduced because the mass M is now the mass of the whole crystal. The recoilless fraction f is expressed as

$$f = \exp(-\frac{E_\gamma \langle x^2 \rangle}{\hbar^2}), \tag{3.1.2}$$

where $\langle x^2 \rangle$ is the mean-square thermal displacement of the nucleus, E_γ the energy of the γ-ray and $\hbar^2 = h/2\pi$ where h is the Planck's constant. When E_r becomes negligibly small compared to the transition energy E_T resonant emission and absorption can easily occur [48]. The transition energies of the identical emitter and the absorber nuclei are given by

$$E_T = E_{excited} - E_{ground} = E'_{excited} - E'_{ground} \tag{3.1.3}$$

where $E_{excited}$ and E_{ground} are the excited and ground state, respectively for recoilless emission. $E'_{excited}$ and E'_{ground} are excited and ground state, respectively for resonance absorption.

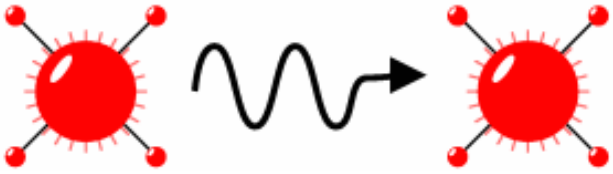

Figure 3.1.3: Recoilless emission or absorption of a gamma ray [49].

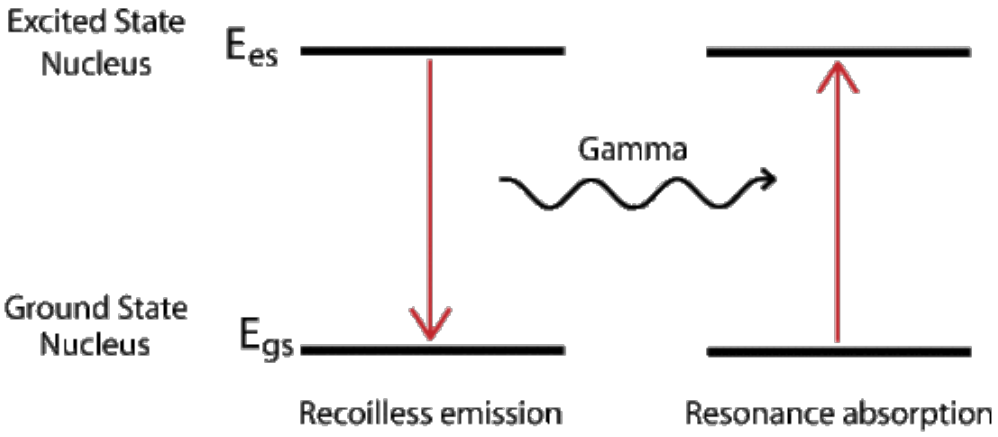

Figure 3.1.4: Graphical representation of resonant absorption and recoilless emission [50].

As illustrated in Figure 3.1.4, the resonant absorption occurs to excite a nucleus from the ground state. A photon energy $E_T = E_{excited} + E_R$ is necessary for Fe^{57}, E_{es} =14.41 keV and $E_R = 2 \times 10^{-2}$ eV. The uncertainty in time corresponds to the mean-life τ of the nuclear state and the uncertainty in energy corresponds to the linewidth Γ of the γ-ray [39]. The relation of these parameters are are given in terms of Heisenberg relation by

$$\Gamma = \frac{\hbar}{\tau}. \tag{3.1.4}$$

When $E_R > \Gamma$, resonant absorption does not occur. The condition for resonant absorption is satisfied when the mass in equation (3.1.1) is much larger, so that $E_R \approx 0$ and $E_T \approx E_\gamma$. Hence Doppler shifting the γ-ray energy by vibrating the source is commonly used for achieving resonant absorption in Mössbauer spectroscopy measurements. The Doppler shifts of γ-ray energies can be shown to be

$$\delta E = E_r \frac{v}{c} \tag{3.1.5}$$

where v is the velocity of the vibrating source usually of about 10 mm/s [51]. A Mössbauer spectrum is a plot of the transmitted intensity against velocity v. Using the appropriate Mössbauer analysis software such as Recoil or MossWinn, the magnetic state of the sample can be deduced from the spectra. For the present work,

the Recoil Mössbauer analysis software was used.

3.2 Hyperfine interactions

Hyperfine interactions are electric or magnetic interactions that exist between a nucleus and its environment. These interactions help to characterize the magnetic state of the material by the generating information for the isomer shift δ, quadrupole splitting Δ and hyperfine magnetic field H. These three hyperfine parameters are very useful quantities for the characterization of materials by Mössbauer spectroscopy [52].

3.2.1 Isomer shift

Isomer shift is the electrostatic energy shift of a nuclear level, due to the finite size of the nucleus and the penetration of electronic charge into the nuclear volume [53]. The shift is caused by a difference in chemical environment between source and absorber [51]. When the valence state of the Mössbauer atom changes, the isomer shift will also change. Thus making it possible to estimate the fraction of Mössbauer isotope in different valence states originating from different crystallographic site occupancies or from the presence of multiple phases in a sample [52]. The shift can be observed in the centroid of a Mössbauer spectrum from the zero velocity centre. It can either be to the left or to the right depending on the energy difference in the electron charge density. The isomer shift is expressed as the difference in the nuclear state between the source (S) and the absorber (A) nuclei in the form of

$$\delta = E_A - E_S. \tag{3.2.1}$$

Then the approximate isomer shift value with Doppler velocity is expressed as

$$\sigma = \frac{2\pi}{5} Ze^2(|\psi(0)|_A^2 - |\psi_S(0)|_S^2)(R_{ex}^2 - R_g^2) \tag{3.2.2}$$

where Z is the atomic number, e is the electron charge, $|\psi(0)|_A^2$ and $|\psi_S(0)|_S^2$) are the s-electron densities of the absorber and the source respectively. R_{ex}^2 and R_g^2 are

the radii of the excited and ground states, respectively. A Mössbauer spectrum is usually first calibrated using an iron foil and reporting of isomer shift tends to be relative to the standard absorber.

3.2.2 Quadrupole splitting

The quadrupole interaction is caused by an electric quadrupole moment. The splitting of the nuclear energy levels as a result of the interaction of the nuclear quadrupole moment with the electric field gradient is called the quadrupole splitting [54]. Peaks of the transmission spectrum splits into two doublets. The separation between the two peaks is then called the quadrupole splitting and is expressed as

$$\Delta = \frac{eV_{zz}Q}{2}. \tag{3.2.3}$$

The expression relates the quadrupole moment Q and the electric field gradient V_{zz} and is given in the units of mm/s. Figure 3.2.1 shows a diagram of the isomer shift, electrical quadrupole splitting and magnetic hyperfine splitting on nuclear energy levels. The excited state $I_{ex} = 3/2$ splits into two sub-levels $\pm 1/2$ and $\pm 3/2$ [51].

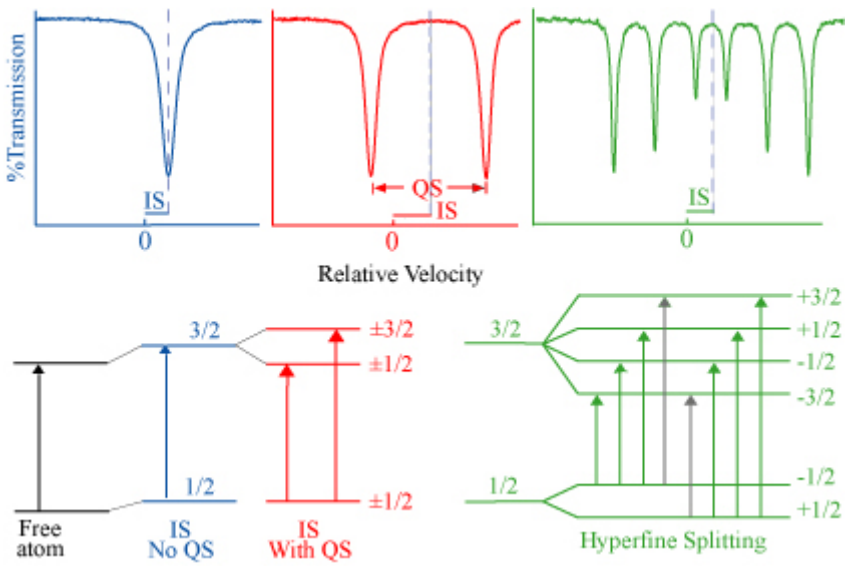

Figure 3.2.1: Isomer shifts, electrical quadrupole splitting and magnetic hyperfine splitting on nuclear energy levels [50].

3.2.3 Magnetic hyperfine interaction

The spin in the nuclear states is associated with the magnetic dipole moments. The spins can be oriented with different projections along a magnetic field direction. The transitions in the nuclear energy is therefore modified when the nucleus is in a magnetic field. The energy perturbations caused by this magnetic interaction are sometimes called the nuclear Zeeman splitting [52]. The splitting that occurs in the magnetic field yields a sextet. The Hamiltonian describing the interaction is given by

$$H_c = -\bar{\mu}.\bar{H} = -g\mu_N \bar{I}.\bar{H} \tag{3.2.4}$$

where μ_N is called the nuclear Bohr magneton and g is the nuclear gyromagnetic ratio also known as the g-factor [48]. The value of μ_N is 5.04929 x10^{-27} J T^{-1} [51]. The energy levels are split into equally non-degenerate energy sub-levels by the magnetic field as shown in Figure 3.2.1.

Chapter 4

Experimental techniques

4.1 Introduction

The properties of nanoferrites are mostly affected by synthesis methods. Wet chemical synthesis methods such as hydrothermal, glycol-thermal and co-precipitation have been reported to be more successful compared to the solid state method [10]. In the present work, the glycol-thermal method was used to synthesize the samples. This method produces a single phase material with small crystalline sizes ranging from 5 nm - 13 nm at a temperature of 200 °C. The single phase formation of the nanoferrites were confirmed by X-ray diffraction (XRD).

4.1.1 Glycol-thermal

The glycol-thermal method is a synthesis method that uses stoichiometric precursors of metal chlorides that are dissolved in de-ionized water to form a mixed solution of starting compounds. $CoSn_xFe_{2-x}O_4$ and $M_{0.5}Ni_{0.5}Fe_2O_4$ nanoparticles were synthesized by the glycol-thermal reaction. The chemical reagents used were $CoCl_2.2H_2O$ (98%), $SnCl_2.2H_2O$ (98%), $MgCl_2.6H_2O$ (99%), $CaCl_2.6H_2O$ (99%), $BaCl_2.2H_2O$ (98%), $SrCl_2.2H_2O$ (98%), $Ni(NO_3)_2.2H_2O$ (99%) and $FeCl_3.6H_2O$ (98%). All chemicals were of analytical grades. These were weighed in required proportions and mixed using a magnetic stirrer for about 30 minutes. In 5 M solution of excess NaOH was then slowly added to the mixture of chloride solutions under rapid stirring until

a pH$\backsim$ 10 was measured by a model 211 microprocessor pH meter. The precipitate was washed several times by deionised water over a Whatman glass mirofibre (GF/F) until there were no traces of the chlorides. A solution of silver nitrated was used to check the presence of the chlorides. The precipitate was then washed by 200 ml of ethanol. The clean precipitate was dispersed in 300 ml of ethylene glycol under rapid stirring. The mixture was then placed in a 600 ml stainless steel pressure vessel (Watlow series model PARR 4843 reactor) as shown in Figure 4.1.1. The temperature was allowed to rise to 200 °C and the gauge pressure was allowed to gradually rise to about 100 psi at 300 rpm. These conditions were held for 5 hours, as shown in Figure 4.1.2. After 5 hours of boiling, the pressure reactor was allowed to cool down to room temperature for an hour. The remaining products were washed over a Whatman glass mirofibre (GF/F) by deionized water then by ethanol. The recovered synthesized sample was dried overnight under a 250 W infrared lamp. The agate mortar and pestle was used to homogenize the recovered sample.

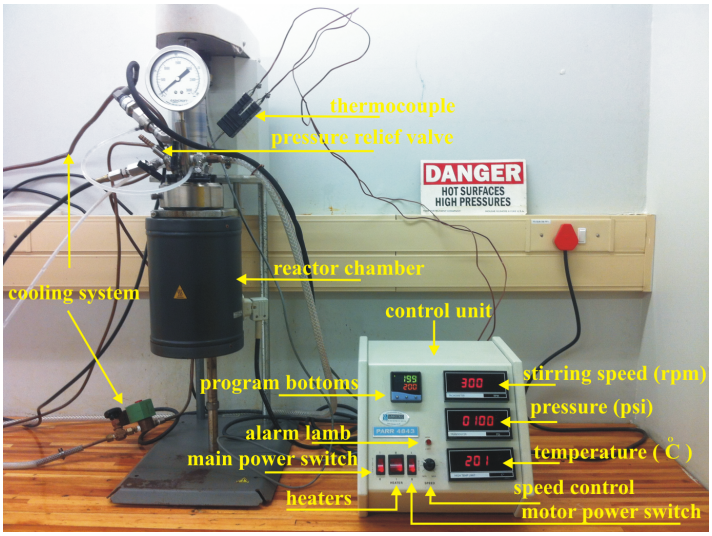

Figure 4.1.1: The PARR 4843 stirred pressure reactor.

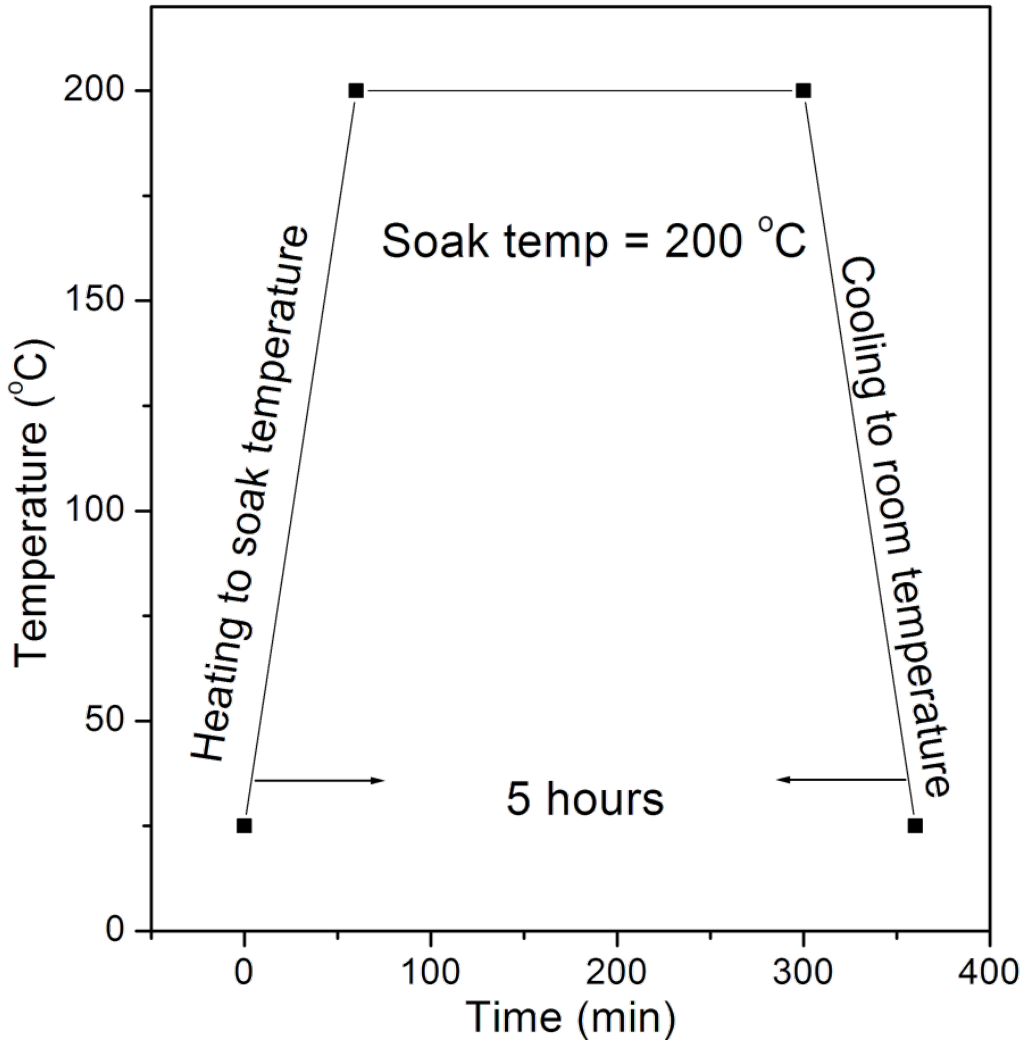

Figure 4.1.2: Synthesis schedule for the PARR 4843 stirred pressure reactor.

4.1.2 X-ray diffraction

X-ray diffraction (XRD) is a structural characterization technique used for the identification of the crystalline structure, different phases and purity of a sample in powder form. If an XRD pattern is found that is not known in the diffraction data libraries an attempt can be made to index the pattern. XRD is based on the use of a monochromatic beam of X-rays with wavelength λ in the range: 0.01-10 nm to probe the material. The analysis of the XRD data is based on Bragg's law

$$n\lambda = 2dsin\theta \tag{4.1.1}$$

where n is the integer, d is the interplanar distance, θ is the angle between the incident beam and the scattering plane and λ is the wavelength of the incident beam. The width of an XRD is related to the grain size D by the Debye-Scherrer [55] formula given by

$$D = \frac{K\lambda}{W_{hkl}cos\theta} \tag{4.1.2}$$

where K is the crystal shape factor, λ is the wavelength of the monochtomatic X-ray beam, W_{hkl} is the line broadening of the diffraction peak at its full-width at half maximum (FWHM) and θ is the Bragg's angle. X-ray density of a sample can be estimated from the XRD measurents with the use of the formula

$$\rho_{XRD} = \frac{8M}{N_A a^3} \tag{4.1.3}$$

where M is the molecular weight of the sample and N_A is the Avogadro's number and a is the lattice parameter calculated and 8 is the number of atoms per unit cell of the spinel lattice. Figures 4.1.3 and 4.1.4 shows the instruments used for the XRD measurements.

Figure 4.1.3: Rigaku Miniflex 600 XRD diffractometer using Cu-K_α radiation (λ = 1.5818 Å).

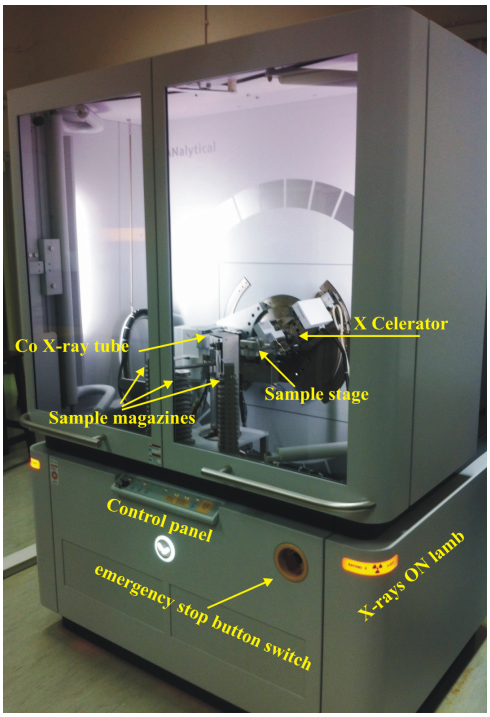

Figure 4.1.4: XRD PANalytical Emperian diffractometer using Co-K_α radiation (λ = 1.7903 Å).

4.1.3 FTIR

(FTIR) is defined as a non-dispersive method of infrared spectroscopy Fourier Transform InfraRed [56]. The mathematical Fourier transform can be expressed as

$$F(\omega) = \int_{-\infty}^{\infty} f(x) e^{i\omega x} dx \tag{4.1.4}$$

and the reverse transform is given by

$$F(x) = \frac{1}{2\pi} \int_{-\infty}^{\infty} f(\omega) e^{i\omega x} d\omega \tag{4.1.5}$$

where ω is the angular frequency, x is optical path difference, $f(x)$ is the interferogram and $f(\omega)$ is the spectrum. $f(x)$ can be determined experimentally and $f(\omega)$ can be obtained by using the Fourier transform [57]. In the infrared (IR) spectroscopy radiation is passed through the sample. Some of that radiation will be absorbed and some will be transmitted. The resulting spectrum represents the molecular fingerprint of the sample. The word fingerprint is used to highlight that each material is a unique combination of atoms and cannot reproduce the same infrared spectrum [58]. In an FTIR (see Figure 4.1.6) instrument, the monochromator and the slits are replaced by an interferometer usually of Michelson type. In the interferometer, a beam of radiation is divided into two beams by means of a beam splitter. The path difference between the beams is introduced where upon they are allowed to recombine. In this way, interference between the beams is obtained and the intensity of the output beam from the interferometer can be monitored as a function of path difference using an appropriate detector. The schematic diagram is shown in Figure 4.1.5.

Some uses of the FTIR include chemical analysis to help match the spectra to unknown databases and monitor chemical reactions on site. It is also used to determine the quality or consistency of a sample, to determine the chemical groups to measure optical conductivity [59, 60]. Some of the advantages of the FTIR is its ability to provide measurements in lesser time, the optical throughput is higher resulting in lower noise levels and mechanical simplicity, the instrument is self-calibrating and never has to be calibrated by the user and measurements are accurate and repro-

ducible [58]. To get the spectra the sample is loaded on the silver plate such that it covers the crystal at the centre. The handle is used to lock the sample and the crystal. The handle is turned clockwise until the reading the about 120 psi. The spectra is generated after a minimum time of 2 minutes. The results for the current study were obtained from the PerkinElmer Spectrum 100 FT-IR spectrometer found in the School of Chemistry and Physics at UKZN Westville campus.

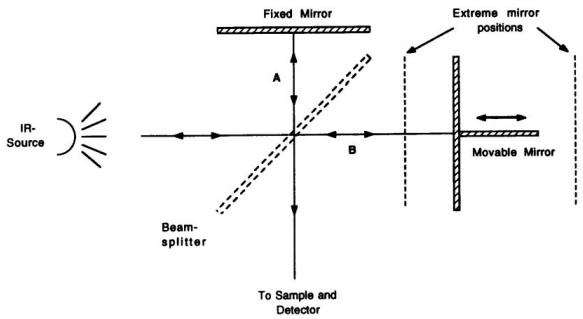

Figure 4.1.5: Schematic diagram of the optical layout of a Michelson interferometer [57].

Figure 4.1.6: PerkinElmer Spectrum 100 FT-IR spectrometer.

4.1.4 HRTEM

High resolution transmission electron microscopy (HRTEM) is a well established technique in the field of research and technology that is used to obtain particle size, orientation and the appearance of the structure. One can also obtain the diffraction pattern of the sample and the concentration of the elements in a sample [61]. The principal set-up of TEM is such that the sample is illuminated with the electrons beams. The formation of the image is generated from the interaction of the electron beans transmitted through a thin sample. The image of the sample is then magnified by means of projection lenses and represented on a screen. The Joel-JEM-2100 high resolution transmission was used is shown in Figure 4.1.7. A small sample of about 0.0002 g was dispersed in ethanol and vibrated in a 40 sonic cleaner for 5 minutes. A copper thin film sample holder is dipped into the dispersed sample and loaded in the HRTEM equipment.

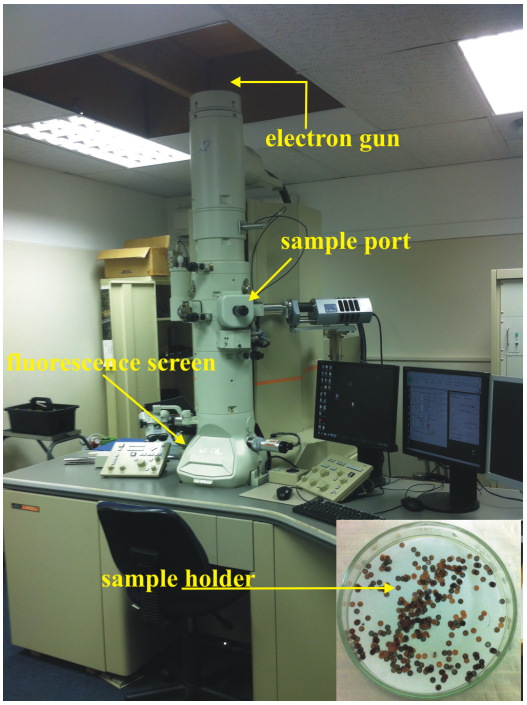

Figure 4.1.7: HRTEM taken at the Electron Microscopy unit at UKZN-Westville campus.

4.1.5 Magnetization measurements

Magnetic measurements were obtained from LakeShore Cryotronics 735 Vibrating Sample Magnetometer (VSM) with an EM4 Electromagnet with Stand and Chiller and a Model 642 Bipolar Power Supply, as shown in Figure 4.1.8. In order to generate a signal proportional to the magnetic moment, the sample is set to vibrate in a constant applied field to a maximum value of about 15 kOe. The signal is detected by an astatic pair of pick-up coils. The coils sense the variation of magnetic flux due to the sample movement. The pick-up coils are located on the poles of the electromagnet. The signal is detected by a lock-in amplifier. The VSM measures the magnetic behavior of a sample as a function of magnetic field, temperature and time. The VSM operates on the basis of Faraday's law of induction which The law states that the induced voltage in the pick-up coils is equal to the negative rate at which the magnetic flux through the loop is changing with time [62] and is expressed as

$$\varepsilon = -\frac{d\phi_B}{dt}. \tag{4.1.6}$$

The magnetization of the sample produced is assumed to be proportional to the induced signal in the pickup coils [62]. The magnetization was calibrated by the use of standard nickel sample sphere with a saturation magnetization of 54.7 emu/g [63]. To take measurements the sample is placed in a cylindrical sample holder and then screwed to the lower end of the vibrating sample rod. The rod is lowered into the sample space to a position between the pick-up coils. The measurements take about an hour to complete. The data is collected using the interface card and the data acquisition software already installed on the computer.

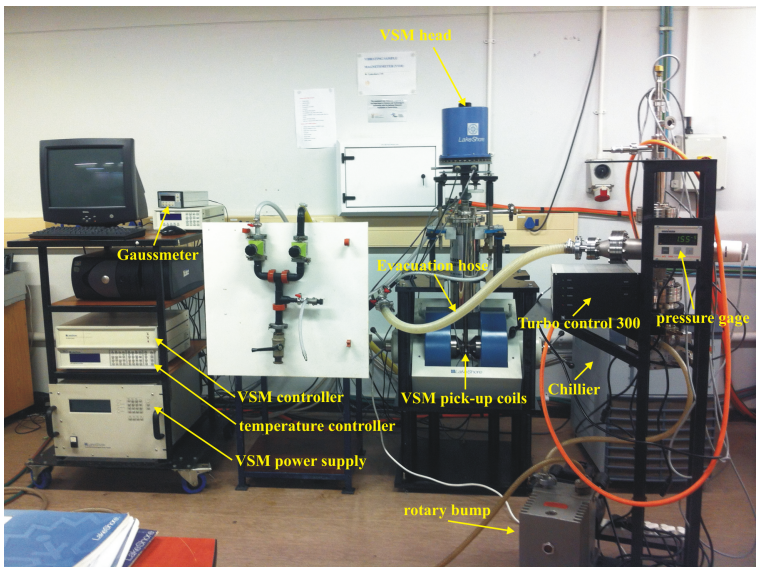

Figure 4.1.8: LakeShore Cryotronics 735 Vibrating Sample Magnetometer.

Chapter 5

Structural and magnetic properties of $CoSn_xFe_{2-x}O_4$ nanoferrite

5.1 Introduction

Superparamagnetism is a unique feature of magnetic nanoparticles. This phenomenon is indicated by blocking behavior characterized by a blocking temperature (T_B), marking a transition to superparamagnetic state. In magnetization measurements blocking behavior is shown as a hump in the zero field cooled (ZFC) curve or zero coercive fields and residual magnetization in hysteresis curves. Mössbauer measurements show onset of superparamagnetism by a transition of Mössbauer pattern from sextet to a doublet. For a collection of magnetic nanoparticles, T_B depends on particle size, anisotropy and interactions in the sample. According to the conventional theory of ferromagnetic nanoparticles, blocking temperature is related to particle volume (V) and anisotropy energy density constant (K) [64] as

$$T_B = \frac{KV}{25k_B}. \tag{5.1.1}$$

The magnetization of magnetic nanoparticles is dependent on the magnetocrystalline anisotropy energy (E_A). Magnetic anisotropy originates from the magnetic coupling

at atomic scale. For a single domain particle, E_A is related to its particle size and anisotropy energy density constant according to the equation

$$E_A = KVsin^2\theta. \tag{5.1.2}$$

The angle θ is between the easy axis of the nanoparticle and applied magnetic field direction. E_A is also related to the energy barrier that will prevent a change in the magnetization direction. Below a critical particle diameter, E_A becomes comparable to nanoparticle's activation energy and an increase in temperature or applied magnetic field can overcome the energy barrier and the magnetization can turn away from its easy axis [65]. Nanomaterials can show remarkably different properties compared to corresponding bulk compounds. Significant changes in properties of nanoparticles can be attributed to a large number of atoms located at the boundary of the crystal due to large surface to volume ratio. Besides particle size, magnetic properties of ferrites are also dependent on the type of cations involved and their distribution and preferences for tetrahedral (A) and octahedral (B) sites in the spinel lattice. The properties of bulk $CoSn_xFe_{2-x}O_4$ compounds produced by standard ceramic process have been reported by V. Vaithyanathan *et al.* [66]. In the study they found that the larger ionic radius of Sn^{4+} resulted in the lattice expansion and the formation of small amount of secondary phase. Here we report on the magnetic properties of $CoSn_xFe_{2-x}O_4$ nanoparticles synthesized by glycol thermal process and characterized by X-ray diffraction (XRD), Mössbauer spectroscopy and magnetization measurements.

5.2 Experimental details

$CoSnxFe_{2-x}O_4$ nanoparticles were synthesized by glycol-thermal reaction.The chemical reagents used were cobaltous chloride $CoCl_2.2H_2O$, stannous chloride $SnCl_2.2H_2O$ and iron (III) chloride hexa-hydrate $FeCl_3.6H_2O$. All chemicals were of analytical grades. The experimental procedure has been discussed in chapter 4. The XRD patterns of the samples were obtained using a monochromatic beam of Co-K_α radiation ($\lambda = 1.7903$ Å) on a model PANalytical Empyrean or Cu-K_α radiation ($\lambda = 1.5818$

Å) on a D8 Brucker advance X-ray diffractometers. The Mössbauer spectra for all the samples was recorded at about 300 K using a conventional constant acceleration Mössbauer spectrometer in transmission geometry with a 25 mCi Co^{57} source sealed in Rh matrix. The standard iron foil was used to calibrate the Mössbauer spectrometer. Variations of the magnetization as a function of applied magnetic field and temperature have been studied by using a Lake-Shore vibrating sample magnetometer (up to 1.4 T and at 300 K) and by a SQUID MPMS produced by Quantum Design (up to 7 T and temperature range 2-400 K).

5.3 Results and discussion

5.3.1 XRD results

The XRD spectra for the as prepared $CoSn_xFe_{2-x}O_4$ (x = 0, 0.1, 0.5 and 1.0) nanosized samples are shown in Figure 5.3.1. All the major peaks are characteristic of pure cubic spinel structure for samples x = 0, 0.1 and 0.5. The shift of the peaks on the sample is accounted to using different XRD models and having different radiation sources Cu-K_α radiation (λ = 1.5818 Å) on a D8 Brucker advance for x = 0 and Co-K_α radiation (λ = 1.7903 Å) on a model PANalytical Empyrean for x = 0.1 and 0.5 and 1.0. Impurity phases have been detected in the sample (x = 1.0). This may be the result of high concentration of large Sn^{2+} ions not being able to fully enter the spinel lattice. Further analysis was carried out for samples x = 0, 0.1 and 0.5 which crystallized with single phase cubic spinel structure. The broad peaks on the XRD spectra for all the samples x = 0, 0.1 and 0.5 indicate smaller particles. The grain sizes shown in Table 5.3.1 were estimated from the 311 XRD peak using the Debye-Scherrer equation. The particle size ranges between 10 nm and 23 nm. The lattice parameters were computed from the XRD data using the formula $a = d\sqrt{h^2 + k^2 + l^2}$ and Bragg's law $n\lambda = 2dsin\theta$. As shown in Table 5.3.1, the unit cell volume increases with increasing Sn content. This is due to substitution of smaller Fe ions by larger Sn ions. The X-ray densities were computed from lattice constants a using the formula [67]. The values of X-ray density shown in Table 5.3.1 are comparable to those reported previously for similar bulk compounds [67, 68, 69].

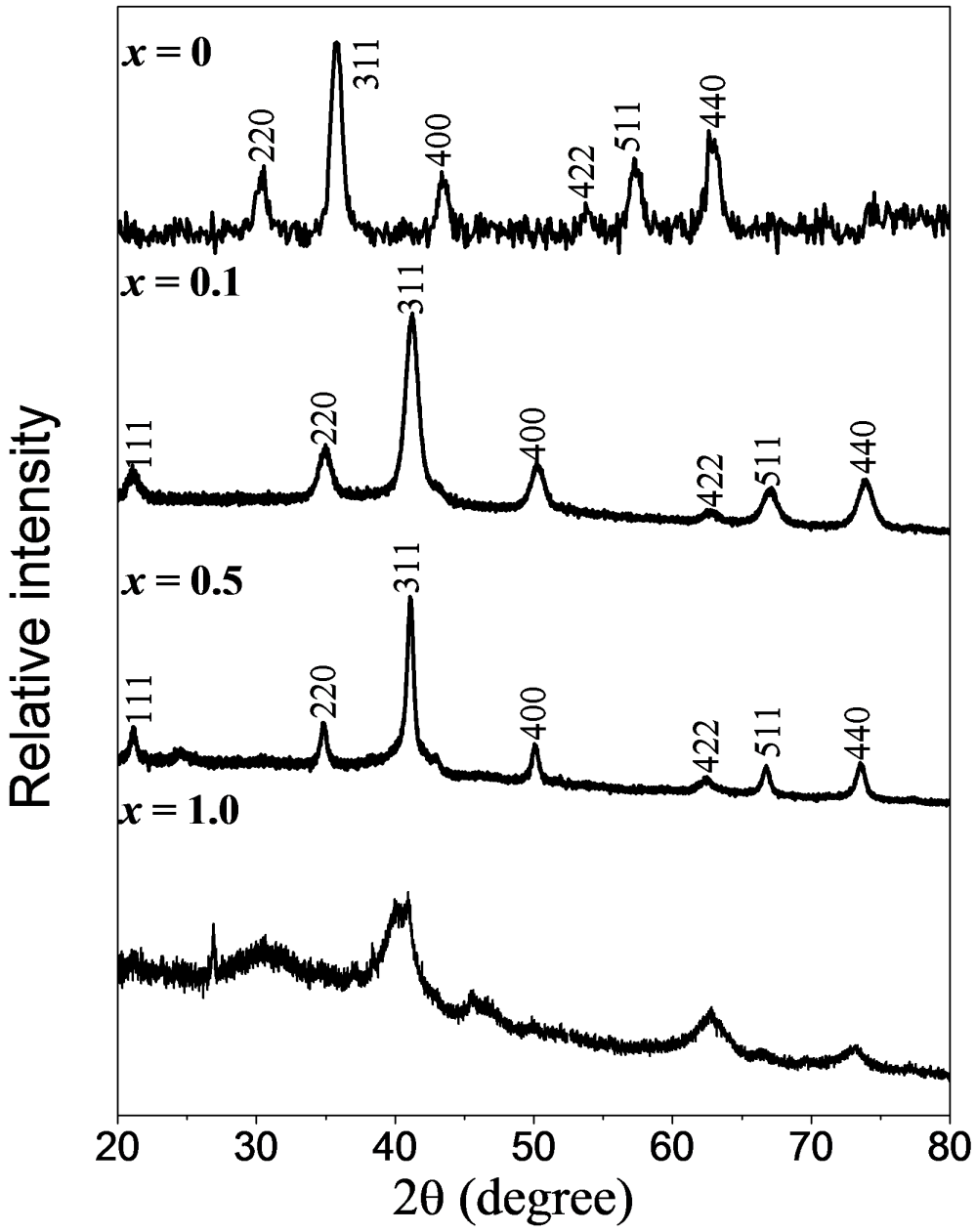

Figure 5.3.1: X-rays patterns for the $CoSn_xFe_{2-x}O_4$ ferrites obtained by Cu-K_α radiation source for $x = 0$ and by Co-K_α for $0.1 \leq x \leq 1.0$.

Table 5.3.1: The lattice parameters (a), crystallite sizes (D), X-ray densities (ρ) and unit cell volume (V) of the ferrites.

x	a (Å)	ρ_{XRD}(g/cm^3)	D (nm)	V(nm^3)
	±0.003	±0.01	±0.2	± 3.0
0.0	8.353	10.5	5.35	582.8
0.1	8.435	11.2	5.33	600.1
0.5	8.463	22.9	5.83	605.1

5.3.2 Morphology study

The morphology and micro-structure of the nanoparticles were investigated using the high energy transmission electron microscopy (HRTEM) and scanning electron microscopy measurements. The typical HRTEM images shows the nanoparticles in Figure 5.3.2. The nanoparticles are nearly spherical with average particle size of about 9.5 nm for the as-prepared sample. Much larger particles can also be identified in the samples. The values of particle size for the $x = 0.1$ and 0.5 estimated from TEM 9.5 nm and 9.9 nm are greater to those from XRD patterns 5.33 nm and 5.83 nm in Table 5.3.1. SEM micrographs shown in Figure 5.3.3 indicates a uniform distribution of particle sizes over a wider distance.

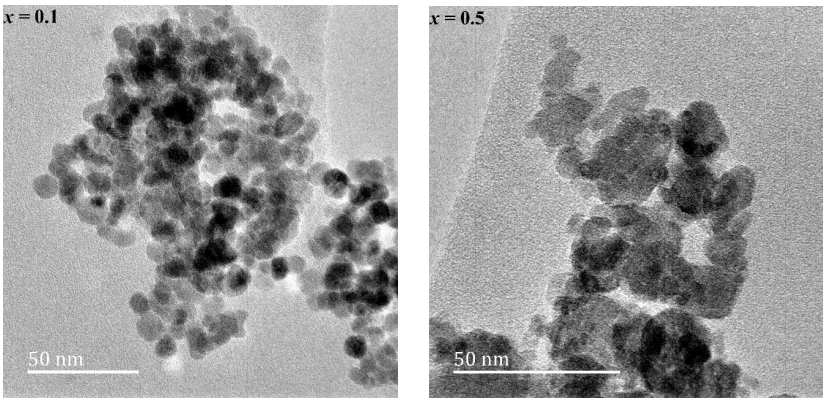

Figure 5.3.2: HRTEM images of $x = 0.5$ and $x = 0.1$.

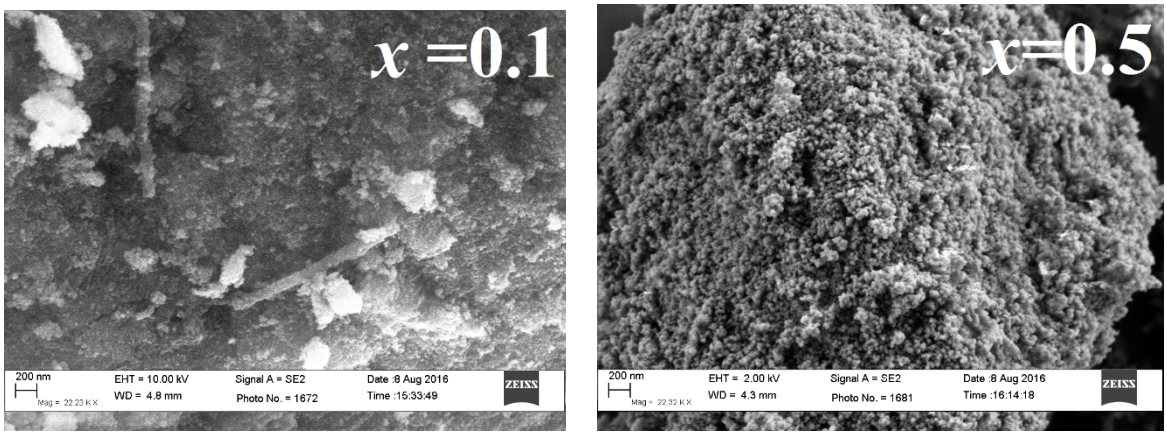

Figure 5.3.3: HRSEM micrographs of $x = 0.5$ and $x = 0.1$.

5.3.3 FTIR results

A typical FTIR spectrum recorded in the frequency range 400 cm^{-1} to 4000 cm^{-1} is shown in Figure 5.3.4 for $CoSn_{0.5}Fe_{1.5}O_4$ ($x = 0.5$). Different bands at about 580, 1050, 1400, 1600, 2300 and 3300 cm^{-1} can clearly be identified. Our plots are from 400 cm^{-1} to cm^{-1} instead of 4000 cm^{-1} to 400 cm^{-1}. This is done consistently as on page 53.

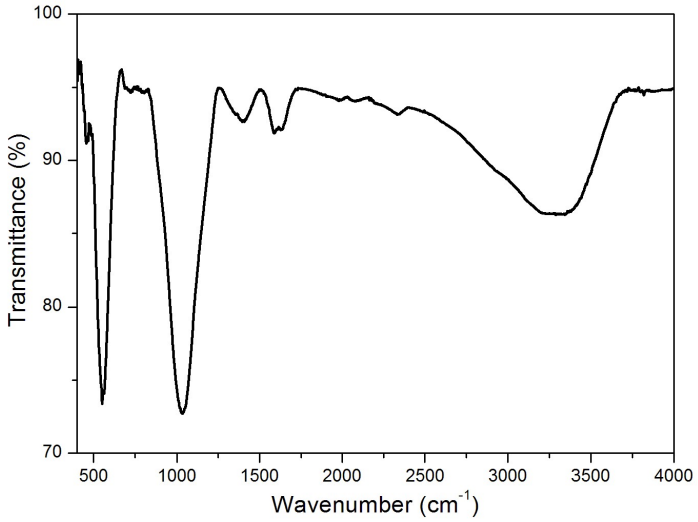

Figure 5.3.4: FTIR spectrum of $CoSn_{0.5}Fe_{1.5}O_4$.

The two strong bands around 580 cm^{-1} and 1050 cm^{-1} appear to be characteristic of single phase cubic spinel structure in agreement with XRD results [69, 70]. The

bands appear shifted to higher frequency due to Sn^{2+}substitution. These absorption bands (associated with low transmittance) are ascribed to the stretching vibration modes of metal-O bonds at the tetrahedral (A) sites and octahedral (B) sites. The high frequency bands at 3300 cm^{-1} and 1600 cm^{-1} are associated with O-H bonds due adsorbed water used in the synthesis process. The band at 2300 cm^{-1} has been identified as due to atmospheric CO_2 while the bands at lower frequancy around 1400 cm^{-1} may be due to carboxyl bonds [69, 70].

5.3.4 Mössbauer measurements

The room-temperature ($\approx$ 300 K) Mössbauer spectra of the oxides are shown in Figure 5.3.5. The observed broad Mössbauer peaks can be attributed to wide particle size distribution. Each particle with a different size will show a different hyperfine magnetic splitting. To fit the spectra three sextets and one doublet were required. The doublet is associated with small nanoparticles in paramagnetic states. The spectrum for nanosized $CoSn_{0.5}Fe_{1.5}O_4$ appears relaxed. It consists of two absorption doublets in addition to six-line component sextets. The additional doublet for this sample was for a better fit. This is indicative of both paramagnetic and ferromagnetic nature of this sample. The fitted data of isomer shifts, hyperfine fields and line widths are shown in Table 6.2.3. There is no significant change in the isomer shifts with composition. This indicates that the s electron density is not significantly affected by Sn concentration. The A- and B-sites isomer shifts in the range 0.29 mm/s to 0.67 mm/s are typical of high spin Fe^{3+} ions [71]. The hyperfine fields for Sn-doped $CoFe_2O_4$ ferrites are lower compared to pure cobalt ferrite oxide. This can be explained by the weakening of superexchange interactions due to dilution of magnetic neighbours (Fe and Co) by nonmagnetic Sn ions. Substitution of Fe ions by Sn leads to tetrahedral ions having few near-neighbour octahedral ions that are magnetic and hence produces a reduction in A-O-B superexchange interactions. The variations of the hyperfine fields associated with different sites are illustrated in Figure 5.3.6 as a function of particle size. In Figure 5.3.7 we show changes at similar sites induced by mechanical milling in a $MnFe_2O_4$ sample. The results appear to show significantly different trends in the changes of the hyperfine fields in relation

to particle sizes.

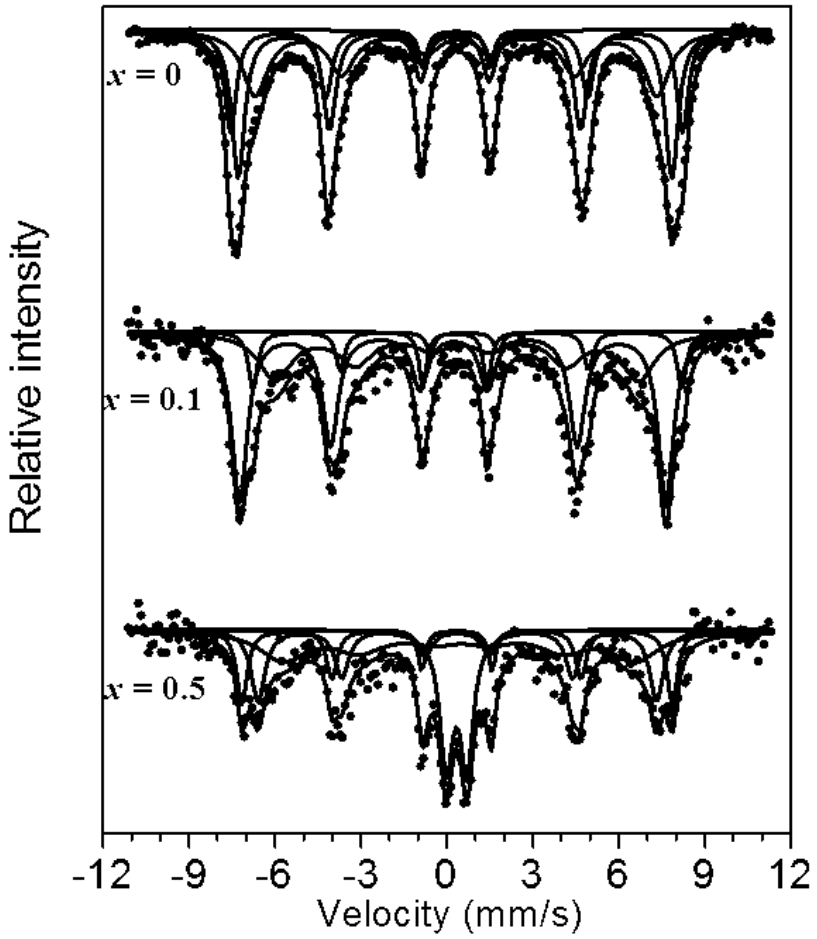

Figure 5.3.5: Mössbauer spectra for $CoSn_xFe_{2-x}O_4$ samples measured at room temperature.

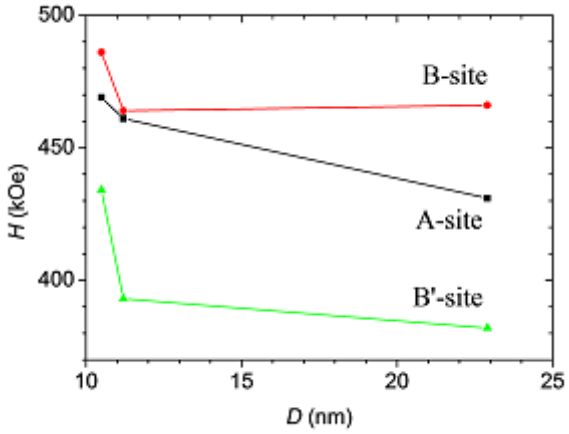

Figure 5.3.6: Hyperfine fields at different sites for $CoSn_xFe_{2-x}O_4$ plotted as a function of particle size.

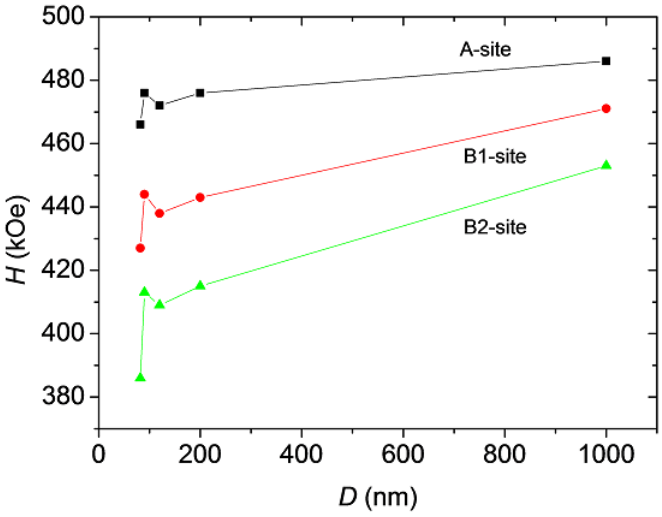

Figure 5.3.7: Hyperfine fields at different sites for $MnFe_2O_4$ plotted as a function of particle size [72].

Table 5.3.2: Isomer shifts (δ), quadrupole splitting (ε), hyperfine fields (H), line widths (Γ) and Fe fraction (f) for $CoSn_xFe_{2-x}O_4$ (x = 0, 0.1, and 0.5).

Ferrite		δ (mm/s)	ε (mm/s)	H (kOe)	Γ (mm/s)	f %
		±0.04	±0.03	±8	±0.04	
$CoFe_2O_4$	A	0.29	0.00	469	0.28	40.7
	B	0.35	0.01	489	0.24	23.4
	B′	0.35	0.03	434	0.53	32.4
	D	0.35	2.33	-	0.17	3.2
$CoSnFe_{2-x}O_4$	A	0.23	-0.02	461	0.33	26.7
	B	0.67	0.05	464	0.19	68.8
	B′	0.42	-0.10	393	0.70	31.5
	D	0.29	2.24	-	0.16	4.6
$CoSn_{0.1}Fe_{1.9}O_4$	A	0.37	0.00	432	0.29	23.7
	B	0.35	-0.03	466	0.22	18.7
	B′	0.48	0.10	382	0.99	33.0
	D_A	0.34	0.71	-	0.27	20.8
	D_B	0.35	2.42	-	0.15	3.6

5.3.5 Magnetization measurements

The hysteresis loops measured at 300 K are shown in Figure 6.2.4. Values of coercive fields, saturation magnetization and residual magnetization estimated from hysteresis loops are also given in Table 5.3.3. The magnetizations M_s reduce from 94.55 emu/g to 13.13 emu/g with increasing Sn concentration. This compares well with the reduction in hyperfine fields with increasing x as indicated by Mössbauer results attributed to fewer magnetic neighbours as a result of substitution of Fe by Sn ions. An increase in coercive field and residual magnetization with increasing x

is observed. Clearly magnetic parameters are affected by Sn concentration.

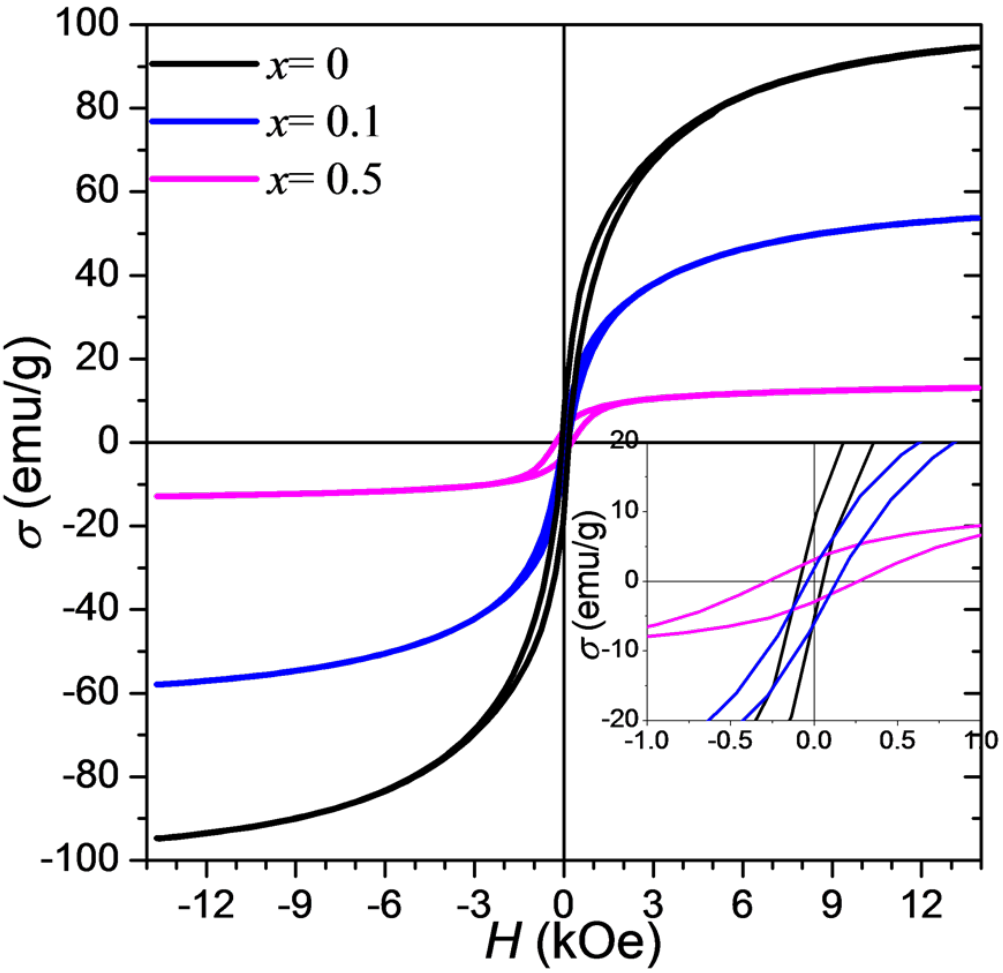

Figure 5.3.8: Hysteresis loops of $CoSn_xFe_{2-x}O_4$ measured at room temperature.

Table 5.3.3: Coercive field H_C, magnetization M_s and residual magnetization M_R measured at 300 K.

x	H_C (Oe)	M_s (emu/g)	M_R (emu/g)
	±0.4	±0.01	±0.001
0.0	73.2	94.55	1.22
0.1	89.1	53.78	1.22
0.5	270.6	13.13	3.11

Figure 5.3.9 shows field dependent initial magnetizations recorded at various temperatures from 4 K to 250 K for $x = 0.5$. The saturation magnetizations increase at lower temperature as expected. The zero field cooled (ZFC) and field cooled (FC) magnetization curves are shown in Figure 5.3.10 for $CoSn_{0.5}Fe_{1.5}O_4$ ($x = 0.5$). During FC, the oxides were cooled from 400 K to 10 K in the presence of an external magnetic field of 50 Oe. In the measurements in Figure 5.3.10, the applied field is zero while cooling to 4 K and the magnetization was recorded during warming up to 400 K in the presence of the same external field of 50 Oe. The magnetization initially increases with increasing temperature and reaches a maximum at a blocking temperature (T_B) of about 300 K. This is higher than the blocking temperature of 238 K reported for $CoFe_2O_4$ which had smaller particle sizes (5 nm) [65].

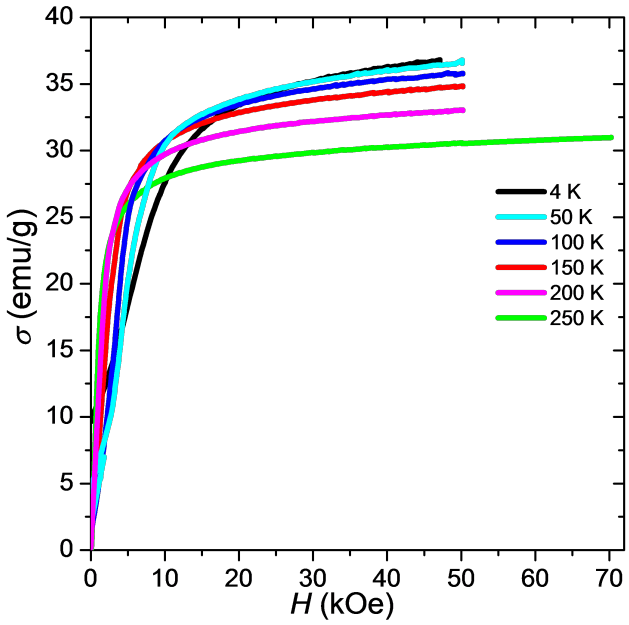

Figure 5.3.9: Magnetization as a function of magnetic field recorded from 4-250 K for x=0.5.

According to the conventional theory of ferromagnetic nanoparticles, larger particles are expected to have higher blocking temperature [64]. The blocking temperature (T_B) is the temperature above which we may expect superparamagnetism to begin. The blocking temperature T_B of 300 K relates well with relaxed Mössbauer spectrum

for $CoSn_{0.5}Fe_{1.5}O4$ recorded at room temperature (300 K). Beyond 300 K, the ZFC magnetization reduces with further increase in temperature. The width of the peak in the ZFC curve is associated with particle size distribution. A particle with a particular size has a certain blocking temperature. The ZFC peak width at half maximum for $CoSn_{0.5}Fe_{1.5}O4$ produced by the glycol-thermal process is 84±1 nm, indicating a narrow particle size distribution.

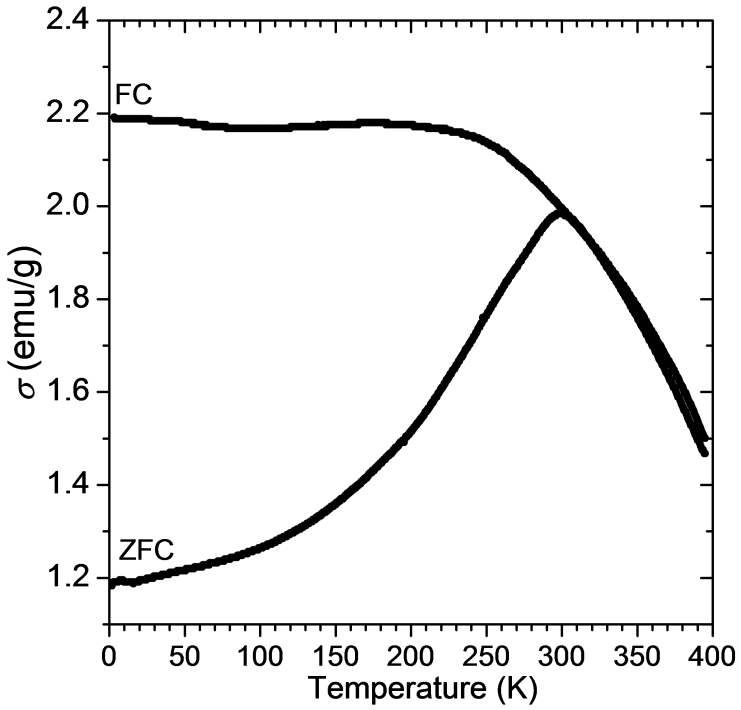

Figure 5.3.10: Zero field cooling magnetization curves.

A strong correlation is shown in Figure 5.3.11 ($\chi^2 = 0.9995$) that is apparent between coercive field data in Table 5.3.3 with particle sizes in Table 5.3.1 which suggests synthesis of other compositions in the current series. The origin of this correlation is the subject for further investigation. The properties of $CoSn_xFe_{2-x}O_4$ are strongly dependent on particle size and Sn content. Sn doping appears to collapse the the magnetic order in $CoFe_2O_4$ in a systematic way exhibiting strong correlation between increase in coercive field and particle size measured at room temperature.

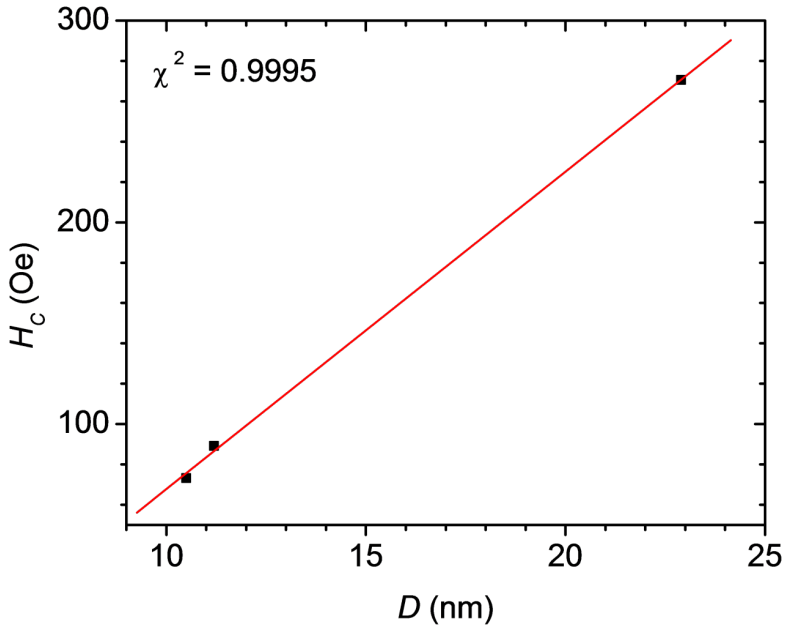

Figure 5.3.11: Correlation between coercive fields at 300 K with crytallite sizes for $x = 0$, 0.1, 0.5.

5.4 Conclusion

$CoSn_xFe_{2-x}O_4$ (x = 0, 0.1 and 0.5) nanoparticles have been characterized by XRD, Mössbauer spectroscopy and magnetization measurements. All the peaks were indexed for a pure cubic spinel structure with no impurity peaks except for the sample with x= 1. Therefore large contents of Sn ions do not enter the structure of $CoFe_2O_4$ as well as when the Sn content was smaller. The properties are strongly dependent on particle size and Sn content. The ZFC magnetizations of $CoSn_{0.5}Fe_{1.5}O_4$ ($x = 0.5$) spin freezing at low temperature. Sn doping appears to collapse the magnetic order in $CoFe_2O_4$ in a systematic way exhibiting strong correlation between increase in coercive field and particle size measured at room temperature. The broad Mössbauer peaks can be attributed to a wide particle size distribution. The hyperfine field of the Sn-doped $CoFe_2O_4$ were found to be lower than the pure $CoFe_2O_4$, this is due to the weakening of the superexchange interactions. The magnetization was decreasing with the increasing Sn concetration, which correlated with the information obtained from the Mössbauer results.

Chapter 6

Synthesis structural and magnetic properties of $M_{0.5}Ni_{0.5}Fe_2O_4$ nanoferrites

6.1 Introduction

Spinel ferrites have been investigated intensively in recent years due to their potential applications in the production of electronic and magnetic components [73]. As stated earlier the distribution of cations over tetrahedral and octahedral sites significantly affect properties which depends on various parameters such as processing conditions, sintering temperature and time on their chemical composition [73, 74]. Several synthesis methods are available and have been used in the preparation of the nanoferrites. Stoichiometric control is not always straightforward. The full control of the pH, temperature and concentration of the solution is often required [73].

The difference of the magnetic moments of the ions from the A and B sites gives rise to the magnetization on both sites. Some studies have shown that the magnetic properties like magnetization, coercivity and remanence may be highly dependent on the size and concentration which affects the strength of the interparticle interaction and anisotropy.Substituting $NiFe_2O_4$ with nonmagnetic metal ions such as Zn^{2+}, Mg^{2+} and Ca^{2+} ions significantly affect the physical properties which may improve or add new properties [74]. This current study will deal with the structural and

magnetic properties of $NiFe_2O_4$ nanoferrites in which the Ni is partially substituted by alkaline earth metals Mg, Ca, Sr and Ba. We will also look at the correlation between coercive field and pressure and coercive field and particle size [75]. The synthesis method used was glycol-thermal. For the structural properties, the samples were characterized by XRD and FTIR. The magnetic properties were characterizes by magnetization VSM and Mössbauer spectroscopy at room temperature.

6.2 Results and discussion

6.2.1 XRD results

In Figure 6.2.1, the XRD patterns for $M_{0.5}Ni_{0.5}Fe_2O_4$ (M= Mg, Ca, Sr and Ba) is shown. The XRD patterns of the samples were obtained using the Rigaku MiniFlex 600 using Cu-K_α radiation (λ = 1.5818 Å). All the major peaks corresponding to the spinel structure are indexed and no impurity peak was observed which implied that the samples made were all single phase. The average crystallite size for each sample was calculated using the Scherrer formula [55]. The crystallite size, lattice parameters and XRD densities are presented in Table 6.2.1. The lattice parameters shows decrease when substituting Mg from 8.355 Å[76] to 8.342 Åand thereafter increases to 8.361 Åwhen substituting Ca. This may be due to the fact that the ionic radii Ca is bigger than the ionic radii of Ni^{2+}. Replacing a cation with a dopant of smaller ionic radius can change the inter-planar spacing that can induce the lattice strain and shift the diffraction peak [77]. The values of the X-ray density ρ_x have been obtained from equation 4.1.3. The density values increases as the metals are substituted, as shown in Table 6.2.1. A strong correlation between particle sizes and pressure for $M_{0.5}Ni_{0.5}Fe_2O_4$ (M= Mg, Ca, Sr and Ba) nanoferrites is shown in Figure 6.2.2. The values of pressure presented in Table 6.2.2 were obtained from the pressure reactor during the synthesis process and they were experimental readings not set intentionally but evolved on their own. This is evident that the samples with larger particle sizes were synthesized at higher pressure. This is consistent with the study by J Gubicza *et al.* [78] who found that at constant temperature the crystallite size increase with pressure. The values for pure $NiFe_2O_4$ were taken from

B. Ndlovu [76].

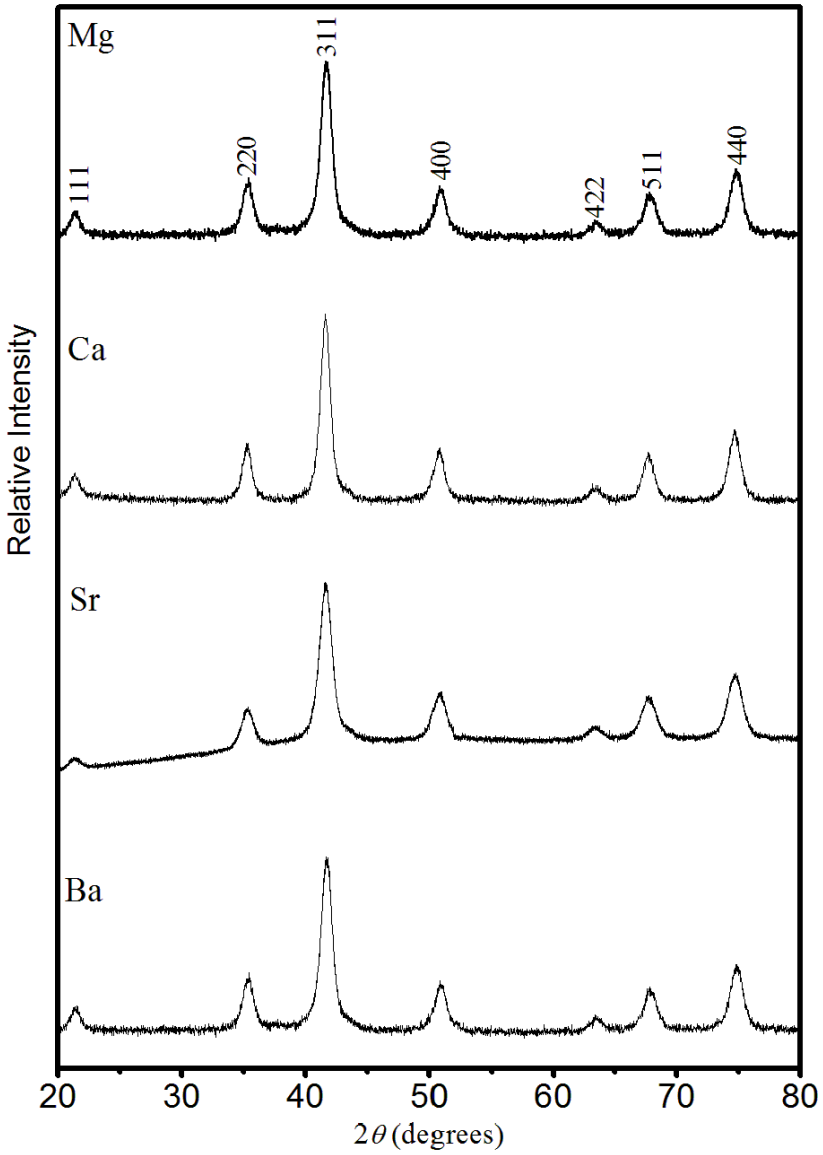

Figure 6.2.1: XRD patterns of $M_{0.5}Ni_{0.5}Fe_2O_4$ (M= Mg, Ca, Sr and Ba).

Table 6.2.1: The lattice parameters (a), crystallite sizes (D), X-ray densities (ρ) of the $M_{0.5}Ni_{0.5}Fe_2O_4$ (M= Mg, Ca, Sr and Ba) ferrites.

Sample	a (Å)	ρ_{XRD}(g/cm^3)	D (nm)
	±0.003	±0.01	±0.2
$Mg_{0.5}Ni_{0.5}Fe_2O_4$	8.342	4.969	11.84
$Ca_{0.5}Ni_{0.5}Fe_2O_4$	8.361	5.116	12.79
$Sr_{0.5}Ni_{0.5}Fe_2O_4$	8.354	5.669	10.17
$Ba_{0.5}Ni_{0.5}Fe_2O_4$	8.341	6.234	11.10

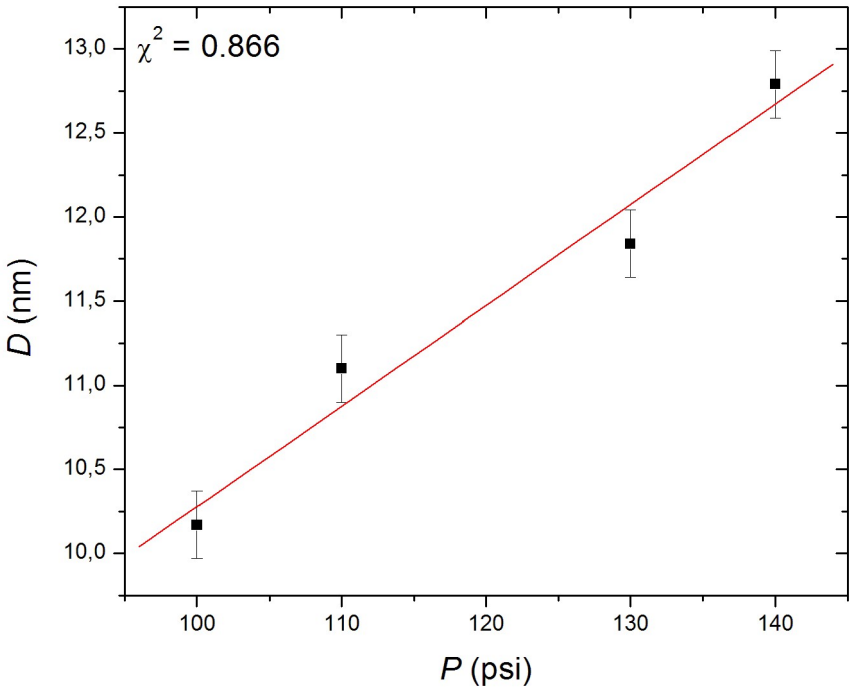

Figure 6.2.2: Correlation between particle size and pressure for $M_{0.5}Ni_{0.5}Fe_2O_4$ where (M = Mg, Ca, Sr and Ba).

6.2.2 FTIR

The formation of the single phase spinel structure of the nanoferrites has been confirmed by the FTIR spectra presented in Figure 6.2.3. The spectra show the absorption bands in the range of 546 cm^{-1}-3285 cm^{-1}. The first band for all the samples range from 546 cm^{-1} -570 cm^{-1} which corresponds with stretching vibration oxygen-metal ions of the tetrahedral and octahedral sites [79]. The peaks around 1595 cm^{-1} - 1654 cm^{-1} corresponds to the H2O molecules [80], as the samples were washed using deionized water. The peaks around 3221 cm^{-1} - 3285 cm^{-1} can be associated with O-H vibrations which are known to vanish after annealing [81].

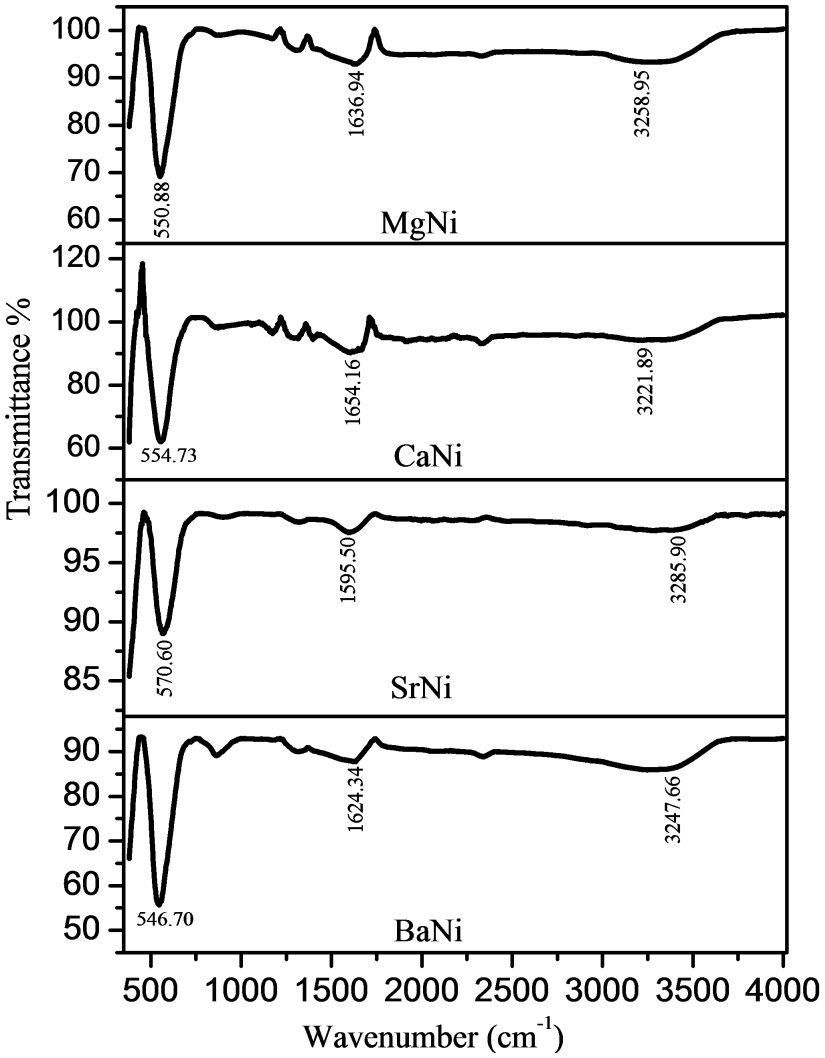

Figure 6.2.3: FTIR spectra for $M_{0.5}Ni_{0.5}Fe_2O_4$ (M= Mg, Ca, Sr and Ba).

6.2.3 Magnetization

Figure 6.2.4 shows the room temperature hysteresis loops for the $M_{0.5}Ni_{0.5}Fe_2O_4$ nanoferrites. The variation of the magnetic parameters are shown in Table6.2.2. The coercive field H_C increases from 12.8 Oe for $NiFe_2O_4$ to 17.3 Oe for Mg-Ni. Then decreases to 13.46 Oe for Ca-Ni and to 12.30 Oe for Sr-Ni. However, there is an increase from 12.30 Oe to 14.6 Oe when Ba is substituted. This may be due to the increase of the superexchange interactions [82]. We can also explain the variation of coercivity with the concentration of the metal ion on the basis of anisotropy field and domain wall energy [83]. The saturation magnetization M_s followed a different trend, there was an increase from 54.1 emu/g for Mg-Ni to 60.4 emu/g for Ca-Ni, this increase may be described on the basis on the noncollinear spin arrangement on the particles' surface [81]. As it can be seen in Figure 6.2.5 the coercive field changes with the change in particle size. This change may be attributed to the exchange coupling between the grains because it induces cooperative demagnetization processes starting from misaligned grains. For multidomain systems the coercivity varies with the grain size [84]. For the highest value of particle size 12.8 nm, the value of the coercive field decreased from 17.3 Oe to 13.5 Oe. This is indicative of a transition of the sample from single domain to a multidomain structure [75].

6.2.4 Mössbauer Spectroscopy results

Room temperature Mössbauer spectra for $M_{0.5}Ni_{0.5}Fe_2O_4$ (M= Mg, Ca, Sr and Ba) nanoferrites have been presented in Figure 6.2.6. The fits were generated based on the Lorentzian site analysis using the recoil Mössbauer analysis software. At least three sextets and a doublet was fitted to the spectra. One corresponds to the Fe^{3+} ions in the tatrahedral A site and the other two magnetic components corresponds to the octahedral B sites with two different avarage nearest neighbor enviroments. The sextet represents the Fe^{3+} ions in ferromagnetic state and a doublet indicates the Fe^{3+} in a ferromagnetic state and the doublet indicates a paramagnetic state [85]. Sextets with higher values of the magnetic field have been assigned to the octahedral site. The Mössbauer parameters from the analysis are presented in Table 6.2.3.

The hyperfine field seems to be decreasing for the samples. This reduction may be explained in terms of collective magnetic excitation. No significant change is observed with isomer shift values, which is true for a ferric ion [86].

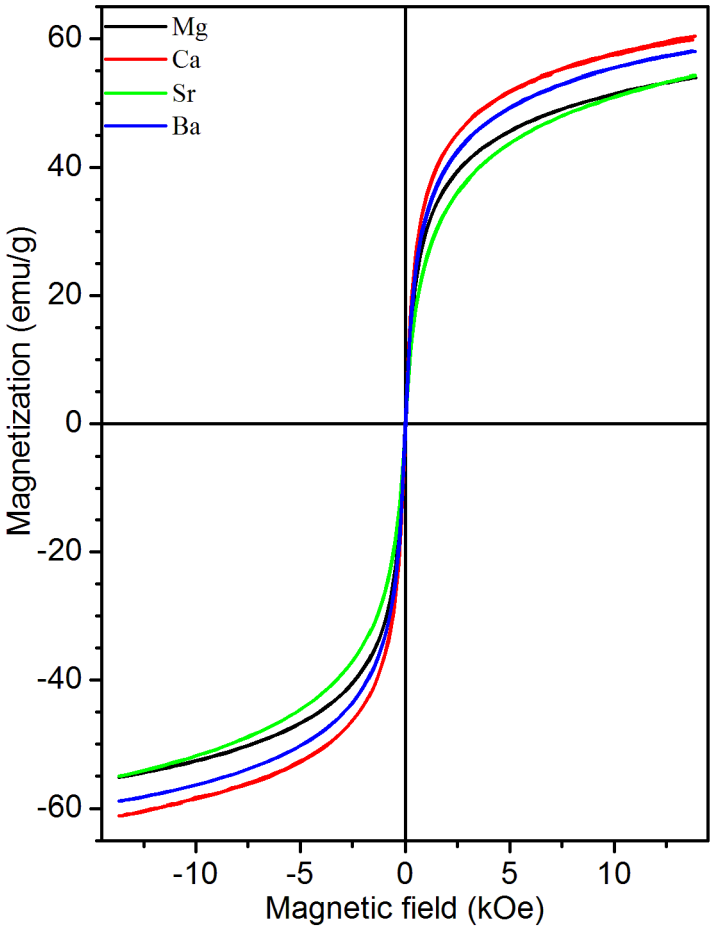

Figure 6.2.4: Hysteresis loops for $M_{0.5}Ni_{0.5}Fe_2O_4$ (M= Mg, Ca, Sr and Ba).

Table 6.2.2: Coercive field H_C, magnetization M_s and residual magnetization M_R measured at 300 K.

Sample	H_C(Oe)	M_s(emu/g)	M_R(emu/g)
	±0.4	±0.01	±0.001
$NiFe_2O_4$	12.83	22.54	0.27
$Mg_{0.5}Ni_{0.5}Fe_2O_4$	17.29	54.06	0.87
$Ca_{0.5}Ni_{0.5}Fe_2O_4$	13.46	60.38	0.86
$Sr_{0.5}Ni_{0.5}Fe_2O_4$	12.30	54.28	0.42
$Ba_{0.5}Ni_{0.5}Fe_2O_4$	14.58	58.16	0.90

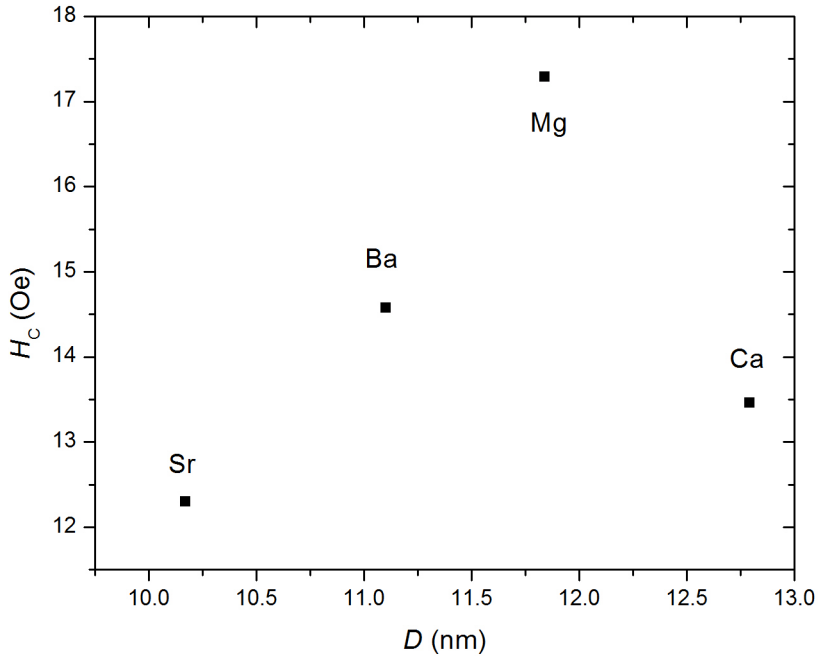

Figure 6.2.5: The variation of coercive field with particle size for $M_{0.5}Ni_{0.5}Fe_2O_4$ (M = Mg, Ca, Sr and Ba).

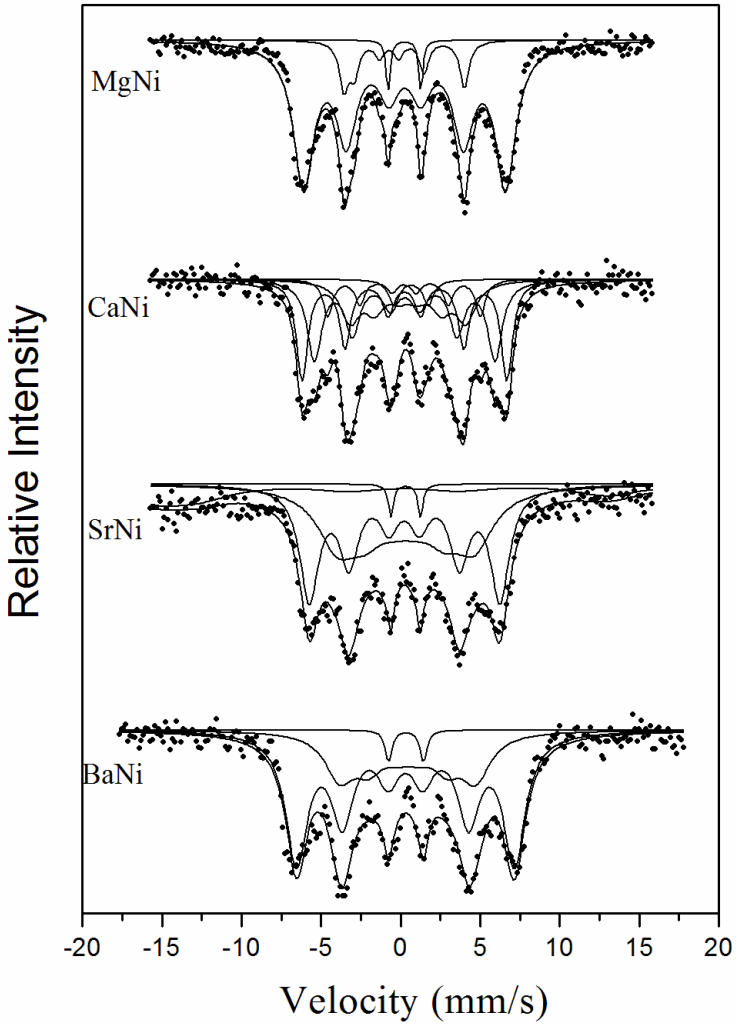

Figure 6.2.6: Mossbauer spectra for $M_{0.5}Ni_{0.5}Fe_2O_4$ nanoferrites.

Table 6.2.3: Isomer shifts (δ), quadrupole splitting (ε), hyperfine fields (H), line widths (Γ) and Fe fraction (f) for $CoSn_xFe_{2-x}O_4$ (x = 0, 0.1, and 0.5).

Ferrite		δ (mm/s)	ε (mm/s)	H (kOe)	Γ (mm/s)	f %
		±0.04	±0.03	±8	±0.04	
$Mg_{0.5}Ni_{0.5}Fe_2O_4$	A	0.35	0.00	398	0.713	37.4
	B	0.30	0.01	461	0.52	46.0
	B′	0.37	0.03	263	0.67	14.0
	D	0.27	2.38	-	0.17	2.6
$Ca_{0.5}Ni_{0.5}Fe_2O_4$	A	0.31	-0.02	381	0.78	38.4
	B	0.27	0.05	445	0.52	34.6
	B′	0.56	-0.10	258	0.90	23.4
	D	0.60	2.46	-	0.47	3.6
$Sr_{0.5}Ni_{0.5}Fe_2O_4$	A	0.27	0.00	303	1.44	49.2
	B	0.26	-0.03	417	0.73	48.9
	B′	0.48	0.10	382	0.99	33.0
	D_A	0.35	2.09	-	0.22	2.0
$Ba_{0.5}Ni_{0.5}Fe_2O_4$	A	0.30		382	0.78	38.4
	B	0.28		445	0.52	34.3
	B′	0.51		255	0.52	38.4
	D	0.48	2.24	-	0.43	3.02

6.3 Conclusion

The nanoferrites $M_{0.5}Ni_{0.5}Fe_2O_4$, (M= Mg, Ca, Sr, Ba) have been successfully synthesized by glycol-thermal. XRD results confirmed single phase formation in all

of the synthesized samples with no impurity peaks. Crystallite sizes ranged from 10 nm to 13 nm. FTIR spectrum confirmed the formation of a spinel structure. Mössbauer spectroscopy results showed that the samples exhibit a ferromagnetic and paramagnetic state with the fit of three sextets and a doublet. There was a strong correlation between the coercive field and particle size and this confirmed the transition of the ferrites from single to multidomain structure. The correlation between synthesis pressure and particle size is confirmed when the pressure increases, the particle size also increases.

Chapter 7

General conclusions

The structural and magnetic properties of $CoSn_xFe_{2-x}O_4$ (x = 0, 0.1, 0.5 and 1.0) and $M_{0.5}Ni_{0.5}Fe_2O_4$ (M = Mg, Ca, Sr, Ba) nanoferrites were successfully produced by glycol-thermal method. Structural properties were investigated by X-ray diffraction which gave the information on crystallite size, lattice parameter and XRD density of all the nanoferrites produced. For all $CoSn_xFe_{2-x}O_4$ (x = 0, 0.1, 0.5 and 1.0) samples a single phase was observed except for x = 1. In this case the spinel structure was not able to form for high concentration of Sn. Therefore, the properties are highly dependent on the particle size and the content of the Sn substitution. In the $M_{0.5}Ni_{0.5}Fe_2O_4$ (M = Mg, Ca, Sr, Ba) samples, all the samples were single phase. The variation of the crystallite sizes showed that the results may not always follow the same trend, we took into consideration the ionic radii of the ions for the elements used. There was a strong correlation between the particle size and synthesis pressure for the $M_{0.5}Ni_{0.5}Fe_2O_4$ ferrite. Larger particles were obtained at higher pressure. The FTIR spectra confirmed the formation of the spinel structure for the ferrites. Room temperature Mössbauer spectra for the ferrites showed an ordered magnetic structure and was fitted with sextets. In other samples, we include doublet component such as for $CoSn_{0.5}Fe_{1.5}O_4$ and $M_{0.5}Ni_{0.5}Fe_2O_4$ (M = Mg, Ca, Sr, Ba). The presence of a doublet was indicative of the ferrites in a paramagnetic phase. The decrease in magnetization with increasing Sn concentration was also consistent with the Mössbauer results. The magnetization measurements for the $M_{0.5}Ni_{0.5}Fe_2O_4$

ferrites showed a nonlinear trend, which was consistent with the Mössbauer and XRD results. The variation between the coercive field and particle sizes for the $M_{0.5}Ni_{0.5}Fe_2O_4$ showed a transition from single domain to multidomain structure. For the future, we intend to investigate further the correlation between coercive field and crystallite size for the Sn-substituted samples. Synthesis at other compositions (x = 0.2, 0.3 and 0.4) for $CoSn_xFe_{2-x}O_4$ will be important to undertake in order to confirm the strong correlation between the coercive fields and crystallite sizes reported in Figure 5.3.11 [15]. All the $M_{0.5}Ni_{0.5}Fe_2O_4$ samples studied here have similar XRD patterns. It would be interesting to see if differences in the properties of the samples can be amplified by performing magnetic measurements at low temperatures.

Bibliography

[1] B. D. Cullity, C. D. Graham, Introduction to magnetic materials, John Wiley and Sons, Inc, Hoboken New Jersey (2009) 175-193.

[2] R. Valenzuela, Magnetic Ceramics, Cambridge University Press, 1994.

[3] E. S. Murdock, R. F. Simmons, R. Davidson, Roadmap for 10Dbit/in 2 Media:Challenge IEEE Trans. Magnetics, 28 **5**(1995) 3078.

[4] V. G. Harris, N. C. Koon, C. M. Williams, Q. Zhang, M. Abe, J. P. Kirkland, Cation distribution in NiZn-ferrite films via extended x-ray absorption fine structure Appl. Phys. Lett. **68** (1996) 2082-2084.

[5] H. K. Hemaunt, J. P. Singh, R. C. Srivastava, P. Negi, H. M. Agrawal and K. Asokan, FTIR and electrical study of dysprosium doped cobalt ferrite nanoparticles, Journal of Nanoscience (2014) 1650-1656.

[6] J. M. D. Coey, Magnetism and Magnetic Materials, Cambridge University Press (2010) 7-8, 24-25, 50-56, 63, 195-203, 330, 329.

[7] U. Müller, Inorganic structural chemistry, John Wiley and Sons, England (1993) 204-208.

[8] P. Sivakumar, R ramesh, A. Ramanand, S. Ponnusamy, C Muthamizhchelvan, Preparation and characterization of $NiFe_2O_4$, Trans. Indian. Inst. Met. **64** (2011) 233-234.

[9] B. P. Ladgaonkar, P. N. Vasambekar, A. S. Vaingankar, Effect of Zn^{2+} and Nd^{3+} substitution on magnetisation and AC susceptibility of Mg ferrite, Journal of Magnetism and Magnetic Materials, **210** (2000) 289-294.

[10] H. F. Abosheiasha and S. T. Assar, Effects of sintering process on the structural, magnetic and thermal properties of $Ni_{0.92}Ca_{0.08}Fe_2O_4$ nanoferrite, Journal of Magnetism and Magnetic Materials, **370** (2014) 54-61.

[11] X. Meng, H. Li, J. Chen, L. Mei, K. Wang, X. Li, Mössbauer study of cobalt ferrite substituted nanocrystals substituted with rare-earth Y^{3+} ions, Journal of Magnetism and Magnetic Materials, **321** (2009) 1155-1158.

[12] A. C. F. M. Costa, E. Tortella, M.R. Morelli and R.H.G.A. Kiminami, Synthesis, microstructure and magnetic properties of Ni-Zn ferrites, Journal of Magnetism and Magnetic Materials **256** (2003) 174-182.

[13] V. S. Sawant and K. Y. Rajpure, The effect of Co substitution on the structural and magnetic properties of lithium ferrite synthesized by an autoco-mbustion method, Journal of Magnetism and Magnetic Materials, **382** (2015) 152-157.

[14] R. Rameshbabu. R. Ramesh, S. Kanagesan, A. Karthigeyan, S. Ponnusamy, Synthesis of superparamegnestic $ZnFe_2O_4$ nanoparticle by surfacant assisted hydrothermal method, J Mater Sci: Mater Electron. **24** (2013) 4279-4283.

[15] N. P. Ngema, J. Z. Msomi, T. Moyo, A. Strydom, D. Britz, Synthesis and magnetic properties of Sn-doped $CoFe_2O_4$ nanoferrites, Journal of superconductivity and Novel Magnetism, (2016) doi:10.1007/s10948-016-3786-6.

[16] A. Lu, E. L. Salabas, F. Schuth, Magnetic nanoparticles: Synthesis, protection functionalization and application, Angew. Chem. Int. Ed. **46** (2007) 1222-1244.

[17] B. P. Jacob, A. Kumar, R. P. Pant, S. Singh, E. M. Mohammed, Influence of preparation method on structural and magnetic properties of nickel ferrite nanoparticles, Bull Mater Sci. **34** (2011) 1345-1350.

[18] C. H. Yan, Z. G. Xu, F. X. Cheng, Z. M. Wang, L. D. Sun, C. S Liao, J. T. Jia, Nanophased $CoFe_2O_4$ prepared by combustion method, Solid State Commun **111** (1999) 287-291.

[19] Y. Liu, M. G. B. Drew, Y. Liu, Preparation and magnetic properties of barium ferrites substituted with manganese, cobalt, and tin, Journal of Magnetism and Magnetic Materials **323** (2011) 945-953.

[20] http://what-when-how.com/electronic-properties-of-materials/magnetic-phenomena-and-their-interpretation-classical-approach-magnetic-properties-of-materials-part-2/ Accessed on 22-03-2017.

[21] N. Varalaxmia, K. V. Sivakumar, Structural and dielectric studies of magnesium substituted NiCuZnferrites for microinductor applications, Materials Science and Engineering B. **184** (2014) 88-97.

[22] M. W. Mukhtar, Muhammad I., I. Ahmad, I. Ali, Majid N. A., M. A. Khan, G. Abbas, M. U. Rana, A. Ali, M. Ahmad, Synthesis and properties of Pr-substituted MgZn ferrites for core materials and high frequency applications, Journal of Magnetism and Magnetic Materials, **381** (2015) 173-178.

[23] J. Young-Wan, P. J. Hyung, J. Hang, L. Wam-Jin, Mater. Sci. Eng. B **147** (2008) 7.

[24] S. W. Silva, T. F. O. Melo, P. C. Morais, Stability of citrate coated magnetite and cobalt ferrite nanoparticles under laser irradiation, IEEE Trans. Magn., **39** (2003) 2645-2647.

[25] A. Gusens, A. Derecke, L Missiaen, D. De Vos, J. Huwyler, A. Eberle, P. De Witte, Int J Cancer, **101** (2002).

[26] M. A. Gabal, Y. M. Al Angari, H. M. Zaki, Structural,magnetic and electrical characterization of Mg-Ni nano-crystalline ferrites prepared through egg-white precursor, Journal of Magnetism and Magnetic Materials, **363** (2014) 6-12.

[27] V. N. Dhange, M. L. Mane, A. P. Keche, C. T. Birajdar, K. M. Jadhav, Physica B **406** (2011) 789-793.

[28] P. C. A. Brito, R. F. Gomes, J. G. S. Duque, M. A Macedo, Physica B, **384** (2006) 91-93.

[29] J. Jiang, L. H. Ai, Physica B, **405** (2010) 2640-2642.

[30] K. Ugender, V. Vaithyanathan, L. N. Patro, S. S. R. Inbanathan, K. K. Bharathi, Temperature-dependent magnetization, anisotropy and conductivity of $CoFe_{2-x}Sn_xO_4$ (x = 0.025, 0.05, 0.075): appearance of grain boundary conductivity at high temperatures, Journal of Physics D: Applied Physics, **49** (2016) 1-10.

[31] A. Repko, J. Vejpravová, T. Vacková, D. Zákutná, D. Nižňanskỳ, Oleate-based hydrothermal preparation of $CoFe_2O_4$ nanoparticles, and their magnetic properties with respect to particle size and surface coating, Journal of Magnetism and Magnetic Materials, **390** (2015)142-151.

[32] K. C. B. Naidu, W. Madhuri, Microwave processed NiMg ferrite: Studies on structural and magnetic properties, Journal of Magnetism and Magnetic Materials, **420**, (2016) 109-116.

[33] T. Vigneswari, P. Raji, Synthesis, characterization and study of photocatalytic activity of $Ni_{0.5}Ca_{0.5}Fe_2O_4$ nanoparticles.

[34] Magnetism "Discovering Science". Gale Research, 1996. Reproduced in Discovering Collection. Farmington Hills, Mich.: Gale Group. December, 2000. http://galenet.galegroup.com/servlet/DC Accessed on 22-03-2017.

[35] J. S. Smart, Effective field theories of magnetism, Philadelphia J.B Saunders company, London (1996) 113-125.

[36] http://hyperphysics.phy-astr.gsu.edu/hbase/solids/magpr.html Accessed on 22-03-2017.

[37] G. N. Mahmoud and B. S. Elias, Crystalization in spinel ferrite nanoparticles, (2012) 357-358.

[38] A. P. Guimaräes, Magnetic and Magnetic Resonance in Solids, John Wiley and Sons, Inc (1998).

[39] M. M. Bruce, Hitchiker's guide to magnetism for the environmental magnetism workshop, Institute for Rock magnetism **279** 48 (1991).

[40] J. C. Maxwell, Magnetic properties of solids, Edinburgh University (1981).

[41] N. W. Ashcroft and N. D. Mermin, Solid state physics, Holt, Rinehart and Winston (1976) 650-652.

[42] C. Kittel, Introduction to solid states physics, 7th edition, John Wiley and sons (1996) 650-652.

[43] N. A. Spaldin, Magnetic Materials: Fundamentals and device applications, Cambridge University Press (2003) 13.

[44] M. McElfresh, Fundamentals of magnetism and magnetic measurements, Purdue University, 1994.

[45] www.springerimages.com Accessed on 22-03-2017.

[46] C. M. Hurd, Contemporary Physics **23** no.5 (1982) 468.

[47] N. S. E. Osman, Synthesis, structural and magnetic charachterization of spinel nanoparticle ferrites with applications for electrochemical sensors, University of KwaZulu-Natal (2015) PhD thesis.

[48] K. W. Gunther, Mössbauer effect: Principles and Applications, Academic Press Inc., New York, London (1964) 3-82.

[49] S. Powers, Molecular Spectroscopy presentation, Wisconsin University, (2004).

[50] M. D. Dyar, D. G. Agresti, M. W. Schaefer, C. A. Grant and E. C. Sklute, Mössbauer spectroscopy and planetary materials, Annual Review of Earth and Planetary Science, **34** (2006) 83-125.

[51] N. N. Greenwood and T. C. Gibb, Mössbauer spectroscopy, Chapman and Hall, London, UK (1971).

[52] F. Brent, Characterization of Materials, John Wiley, New York, (2011).

[53] A. M. Van der Kraan, Mössbauer effect studies of superparamagnetic α-FeOOH and α-Fe_2O_3, Wiley Online Library (1972).

[54] V. D. Perepelitsa, Mössbauer Spectroscopy of ^{57}Fe, MIT Department of Physics, (2007).

[55] A. Hassan, A. K. Muhammad, S. Muhammad, M. Asghar, I. Shakir, S. Naseem, S. Riaz and W. F. Muhammad , Nanocrystalline Zn_{1-x} $Co_{0.5x}Ni_{0.5x}Fe_2O_4$ ferrites: Fabrication via co-precipitation route with enhanced magnetic and electrical properties, Journal of Magnetism and Magnetic Materials, **393** (2015) 56-61.

[56] Thermo Nicolet Corporation, Introduction to fourier transform infared spectrmetry, Thermo Nicolet Corporation:Madison-USA 2001.

[57] B. H. Stuart Infrared spectroscopy:Fundamentals and applications (2004).

[58] T. Woods, FTIR spectroscopy industrial sample analysis, Polymer research centre School of Physics (2012).

[59] L. E. Åmand and J. T. Claes, Theory behind FTIR analysis,department of energy and conversion, Chalmers University of Technology, Götebotg, Sweden (2007).

[60] J. S. Gaffney, N. A. Marley and D. E Jones, Fourier Transform Infrared (FTIR) spectroscopy. Characterization of Materials (2012) 1-33.

[61] A. Tonejc, HRTEM: image processing analysis of defects and grain boundaries in nanocrystalline materials, Acta. Chim. Slov., **46** (1999) 435-461.

[62] W. Burgei, M. J. Pechan and H. Jaeger, A simple vibrating sample magnetometer for use in materials physics course, Am. J. Phys **70** no. 8 (2003)825-828.

[63] J. Swarts,Lake Shore Cryotronics, Inc, 575 MvCorkle Blvd, Westerville, Ohio (2001) 88.

[64] L. Wang, F. S. Li, Mössbauer study of nanocrystalline Ni-Zn ferrite, Journal of Magnetism and Magnetic Materials, **223** (2001) 233-237.

[65] P. Pilišová, J. Kováč, A. Voigt and P. Raschman, Structure and magnetic properties of Co and Ni nano-ferrites prepared by a two step direct microemulsion synthesis, Journal of Magnetism and Magnetic Materials, **341** (2013) 93-99.

[66] V. Vaithyanathan, K. Ugendar, J. A. Chelvane, K. K. Bharathi and S. S. R. Inbanathan , Structural and magnetic properties of Sn and Ti doped Co ferrite, Journal of Magnetism and Magnetic Materials, **382** (2015) 99-92.

[67] W. R. Agami, A. A. Sattar, Structural, IR and magnetic studies of annealed Li-ferrite nanoparticles, J. Mater. Eng, **23** (2014) 604-610.

[68] W. A. Maher, M. Bakr, Structural and magnetic characterization and cation distribution of nanocrystalline $Co_xFe_{3-x}O_4$, Journal of Magnetism and Magnetic Materials, **378** (2015) 246-252.

[69] W. B. Dlamini, J. Z. Msomi and T. Moyo, XRD, Mössbauer and magnetic properties of $Mg_xCo_{1-x}Fe_2O_4$ nanoferrites, Journal of Magnetism and Magnetic Materials, **373** (2015) 78-82.

[70] S. A. Elkady, S. I. Hussein and R. M. Mohamed, Structural and magnetic properties of Gd^{3+} ion substituted magnesium ferrite nanopowders, Journal of Magnetism and Magnetic Materials, **385** (2015) 70-76.

[71] A. Pradeep, P. Priyadharsini and G. Chandrasekaran, Sol-gel route of synthesis of nanoparticles of $MgFe_2O_4$ and XRD, FTIR and VSM study Journal of Magnetism and Magnetic Materials, **320** (2008) 2774-2779.

[72] H. Mahmoud, H. H. Hamdeh, C. J. Ho, M. J. O'Shea, J. C. Walker, Mössbauer srudies of manganes ferrites fine particles processed by ball milling Journal of Magnetism and Magnetic Materials, **220**(2000) 139-146.

[73] Z. K. Heiba, Y. Mostafa Nasser and H. A. Omar , Structural and magnetic properties correlated with cation distribution of Mo-substituted cobalt ferrite nanoparticles, Journal of Magnetism and Magnetic Materials, **368** (2014).

[74] N. Singh, A. Agarwal, S. Sangh and S. Khasa, Dielectric loss, conductivity relaxation process and magnetic properties of Mg substituted Ni-Cu ferrites , Journal of Magnetism and Magnetic Materials, **324** (2012) 2506-2511.

[75] R. Malik, S. Annapoorni, S. Lamba, V. R. Reddy, A. Gupta, P. Sharma, A. Inoue, Mössbauer and magnetic strudies in nickel ferrite nanoparticles: Effect of size distribution, Journal of Magnetism and Magnetic Materials, **322** (2010) 3742-3747.

[76] B. Ndlovu, Synthesis, structural and magnetic properties of $Ni_xCo1 - xFe_2O_4$ and $CoRE_{0.1}Fe1.9O_4$ nanoferrites, University of KwaZulu-Natal (2017) MSc dissertation.

[77] A. Putnis, Introduction to mineral sciences, University of Cambridge (1992)

[78] J. Gubicza, S. Nauyoks, L. Balogh, J. Labar, T. W. Zerda, T. Ungar, Influence of sintering temperature and pressure on crystallite size and lattice defect structure in nanocrystalline SiC, Journal of Materials Research, **22** (2007) 1314-1321.

[79] A. Zak Khorsand, W. H. M. Abd , M. E. Abrishami and R. Yousefi X-ray analysis of ZnO nanoparticles by Williamson-Hall and size-strain plot methods, Journal of Solid State Sciences, **13** (2011) 251-256.

[80] X. Shouhu, H. Lingyun, J. Wanquan, G. Xinglong, H. Yuan and C. Zuyao, A facile method to fabricate carbon-encapsulated Fe_3O_4 core/shell composites, Journal of Nanotechnology, **18** (2007) 035602.

[81] H. Moradmard, S. Shayesteh, T. P. Farjami, Z. Abbas and M. Khaleghi , Structural, magnetic and dielectric properties of magnesium doped nickel ferrite nanoparticles, Journal of Alloys and Compounds, **650** (2015) 116-122.

[82] N. A. Muhammad, J. I. Muhammad, N. H. Muhammad, H. G. Pablo, M. Q. Ashfaq, Synthesis, magnetic and dielectric properties of Er-Ni doped Sr-hexaferrite nanomaterials for applications in high density recording media and

micowave devices, Journal of Magnetism and Magnetic Materials, **324** (2012) 15-19.

[83] S. Jauhar and S. Singhal, Substituted cobalt nano-ferrites, $CoM_xFe_{2-x}O_4$ (M = Cr^{3+}, Ni^{2+}, Cu^{2+}, Zn^{2+}; $0.2 \leq x \leq 1.0$) as heterogenous catalysts for modified Fenton's reaction, Ceramics International, **40** (2014) 11845-11855.

[84] M. A. Dara, V. Vermaa, S. P. Gairolaa, W. A. Siddiquib, R. K. Singha, R. K Kotnalaa, Low dieletric loss of Mg doped Ni-Cu-Zn nano-ferrites for powder applications, Applied Surface Science, **258** (2012) 5342-5347.

[85] M. A. Gismelseed, K. A. Mohammed, H. M. Widatallah, A.D. Al-Rawas, M. E. Elzain and A. A. Yousif Structure and magnetic properties of the $Zn_xMg_{1-x}Fe_2O_4$ ferrites, Journal of Physics: Conference Series, **217** (2010) 012138.

[86] A. Ghasemi , A. Paesano and C. Machado and C. Fabiana, Structural and magnetic characteristics of $Co_{1-x}Ni_{x/2}Sr_{x/2}Fe_2O_4$ nanoparticles, Journal of Magnetism and Magnetic Materials, **324** (2012) 2193-2198.